Icarus 422 (2024) 116253

Contents lists available at ScienceDirect

Icarus

journal homepage: www.elsevier.com/locate/icarus

Research Paper

Modeling the plasma composition of 67P/C-G at different heliocentric distances

Sana Ahmed *, Vikas Soni

Planetary Sciences Division, Physical Research Laboratory, University Area, Ahmedabad, 380009, Gujarat, India

ARTICLE INFO

Keywords:
Comets
67P/C-G
Rosetta
Plasma
Coma chemistry

ABSTRACT

The *Rosetta* spacecraft accompanied the comet 67P/C-G for nearly 2 years, collecting valuable data on the neutral and ion composition of the coma. The Rosetta Plasma Consortium (RPC) provided continuous measurements of the in situ plasma density while ROSINA-COPS monitored the neutral composition. In this work, we aim to estimate the composition of the cometary ionosphere at different heliocentric distances of the comet. Läuter et al. (2020) derived the temporal evolution of the volatile sublimation rates for 50 separated time intervals on the orbit of 67P/C-G using the COPS and DFMS data. We use these sublimation rates as inputs in a multifluid chemical-hydrodynamical model for 36 of the time intervals for heliocentric distances < 3 au. We compare the total ion densities obtained from our models with the local plasma density measured by the RPC instruments. We find that at the location of the spacecraft, our modeled ion densities match with the in situ measured plasma density within factors of $1-3$ for many of the time intervals. We obtain the cometocentric distance variation of the ions H_2O^+ and H_3O^+ and the ion groups created respectively by the ionization and protonation of neutral species. We see that H_3O^+ is dominant at the spacecraft location for nearly all the time intervals while ions created due to protonation are dominant at low cometocentric distances for the intervals near perihelion. We also discuss our ion densities in the context of their detection by DFMS.

1. Introduction

Comet 67P/Churyumov-Gerasimenko (henceforth 67P/C-G) is a Jupiter family comet that is currently characterized by an orbital period of 6.44 yr, and perihelion and aphelion distances of 1.24 au and 5.68 au, respectively. It was the target of the European Space Agency's *Rosetta* mission (Schulz, 2009) that orbited in its vicinity for nearly 26 months, starting from the first encounter on 6 August 2014 at a heliocentric distance of 3.6 au. The spacecraft subsequently escorted 67P/C-G through the 2-year period that included the comet's arrival at perihelion on 13 August 2015, and then post-perihelion up to the end of the mission on 30 September 2016. *Rosetta* typically remained at cometocentric distances ranging from tens to hundreds of kilometers during the mission period.

The sublimation of volatile ices from the comet nucleus forms the coma. The neutral species in the coma are partially ionized due to photoionization, electron impact ionization, and charge exchange with the solar wind (Cravens et al., 1987), thereby forming the cometary ionosphere. Changes in the comet's heliocentric distance lead to alterations in the cometary outgassing rate and activity patterns. The continuous monitoring of 67P/C-G by the *Rosetta* suite of instruments has enabled studies on the evolution of the coma for varying heliocentric distances and spatial locations, including seasonal variability. Among the instruments carried by *Rosetta* was the Rosetta Orbiter Spectrometer for Ion and Neutral Analysis (ROSINA; Balsiger et al., 2007) that included the Double Focusing Mass Spectrometer (DFMS), the Reflection-type Time-Of-Flight (RTOF) mass spectrometer, and the COmet Pressure Sensor (COPS). While ROSINA-DFMS was able to measure mass spectra in the range of 13–140 uq^{-1} in low and high resolution modes, ROSINA-COPS provided us with time-series measurements of the total neutral density. *Rosetta* was also equipped with the instruments of the Rosetta Plasma Consortium (RPC; Carr et al., 2007) for monitoring the cometary plasma parameters. RPC included the Mutual Impedance Probe (MIP; Trotignon et al., 2007) and the LAngmuir Probe (LAP; Eriksson et al., 2007) that were used to derive the in situ plasma density.

Analyses of the ROSINA-DFMS spectra led to the detection of a large number of different ion species in 67P/C-G. The high resolution mode of DFMS ($m/\Delta m > 3000$ at 1% peak height for 28 uq^{-1}; Balsiger et al., 2007) could distinguish between ions that had very small difference in mass-per-charge ratios, e.g. H_2O^+ and NH_4^+. Beth et al. (2016) report on the first in situ detection of NH_4^+ ions when 67P/C-G was near

* Corresponding author.
E-mail addresses: ahmedsana@prl.res.in, ahmed.sana92@gmail.com (S. Ahmed).

https://doi.org/10.1016/j.icarus.2024.116253
Received 14 February 2024; Received in revised form 1 August 2024; Accepted 4 August 2024
Available online 5 August 2024

perihelion. An ionospheric model given by Vigren and Galand (2013) that solves the continuity equation is used by Beth et al. (2016) to understand the chemistry of NH_4^+ ions for coma conditions encountered in July-August 2015. Beth et al. (2020) report on the in situ detections of cometary ions over the range 13–39 uq^{-1} from data acquired by DFMS in the high resolution mode and the first unambiguous detection of a dication (doubly charged ion) CO_2^{++} in a cometary ionosphere.

Previous studies have used a multi-instrument data-based ionospheric model to quantify the ionization sources in 67P/C-G (Galand et al., 2016; Hajra et al., 2017; Heritier et al., 2017b, 2018). Galand et al. (2016) applied this model to the large heliocentric ($r_h > 3$ au) and low cometocentric distances ($r < 20$ km) during the early mission period (October 2014) and found that solar EUV photoionization and electron impact ionization are the main ionization sources in the coma. Galand et al. (2016) also found variability in the ionization sources with spatial location; while photoionization dominated in the northern hemisphere (summer), the contribution of electron impact ionization had to be taken into account in order to explain the ion density over the southern hemisphere (winter). Heritier et al. (2018) used this model for post-perihelion cases ($r_h > 2.6$ au; March-August 2016), and also found seasonal variability as Galand et al. (2016). Heritier et al. (2018) also found that near perihelion, where the neutral density is the highest, photoionization is the dominant ionizing source, while electron impact ionization is dominant at large heliocentric distances. Hajra et al. (2017) applied the ionospheric model to study the plasma density during a cometary outburst in February 2016, while Heritier et al. (2017b) used it to study the near-surface cometary ionosphere during the final descent of *Rosetta* at the end of the mission (September 2016). Simon Wedlund et al. (2019) found that the ionization due to solar wind charge exchange, though normally less than photoionization by factors of 5–100, may sometimes become higher than the photoionization frequency during transient events such as interplanetary coronal mass ejections.

Although the total ion density can be known from the LAP and MIP measurements (Edberg et al., 2015; Eriksson et al., 2017; Henri et al., 2017; Johansson et al., 2021), it was difficult to directly measure the number density of each ionic species. The narrow field of view of DFMS could only sample a small part of the full ion distribution, and pickup by the solar wind could further deflect the ions from the DFMS field of view (Fuselier et al., 2015). In this work, we aim to estimate the composition of the ionosphere of 67P/C-G at different locations in its orbit around the Sun. For this purpose, we have obtained numerical solutions to a multifluid chemical-hydrodynamical model by varying the input conditions (volatile sublimation rates) at different orbital locations. Our model outputs give us the variation of the densities of assorted ions with cometocentric distance and we compare the total ion densities obtained from our models with the in situ measurements of LAP and MIP. Section 2 describes the modeling approach while Section 3 contains a description of the instrument datasets and the input conditions which we have made use of in this study. The results and discussions are presented in Sections 4 and 5, respectively and the concluding remarks are made in Section 6.

2. The coma model

We use a combined chemical-hydrodynamical model suitable for a coma that is assumed to be spherically symmetric and in a steady state. The model philosophy is given by the multifluid work of Rodgers and Charnley (2002), with subsequent additions given by Weiler (2007) and Ahmed and Acharyya (2021). The gas phase coma is approximated as a fluid; a multifluid approach is adopted, in which the coma is divided into three fluids, namely the ions, the neutrals, and the electrons. These three fluids have individual temperatures and a common bulk velocity. In addition to the creation of ions, radicals, and electrons in the coma due to photodissociation/photoionization, the species in the coma undergo a host of gas-phase chemical reactions, which include ion-neutral and neutral-neutral collisional reactions, dissociative recombination reactions, and electron impact reactions. The energy released due to the chemical reactions is distributed non-uniformly among all of the species, resulting in different temperatures of the ions, neutrals, and electrons, and hence our multifluid approach. The expansion velocity for all species is assumed to be the same. Since the ions and electrons are coupled due to Coulomb interactions, resulting in charge neutrality, the assumption of a common velocity (plasma velocity) for the ion and electron fluids in a spherically symmetric coma is reasonable. In some regions of the coma, the electron temperature can attain very high values ($\sim 10^4$ K), causing the plasma velocity to become subsonic. A smooth transition through the sonic point requires a separate numerical treatment. To avoid this, we assume that the plasma velocity is the same as the velocity of the neutral species so that all of the fluids move with a single bulk velocity (Rodgers and Charnley, 2002; Weiler, 2007; Hölscher, 2015; Ahmed and Acharyya, 2021).

Apart from heat exchange between fluids due to chemical reactions, there is also the exchange of energy by means of elastic and inelastic scattering (for example, ion-electron Coulomb interactions, electron-neutral ro-vibrational excitations of neutral species, and so on). A full model description of all the components that need to be calculated to arrive at numerical solutions is given in Ahmed and Acharyya (2021). The modeling approach is based on obtaining numerical solutions to the equations for the conservation of number density, mass, momentum, and energy. The steady-state and spherically symmetric continuity equation for a species i having number density n_i, bulk velocity v, production rate P_i, and loss rate L_i at a cometocentric distance r, is given by:

$$\frac{1}{r^2}\frac{d}{dr}(r^2 n_i v) = P_i - L_i. \tag{1}$$

The above equation is coupled with the differential equations for the conservation of mass, momentum, and energy, which are given by Eqs. (2), (3) and (4), respectively.

$$\frac{1}{r^2}\frac{d}{dr}(r^2 \rho v) = M, \tag{2}$$

$$\frac{1}{r^2}\frac{d}{dr}(r^2 \rho v^2) + \frac{d}{dr}(n k_B T) = F, \tag{3}$$

$$\frac{1}{r^2}\frac{d}{dr}\left[r^2 \rho v \left(\frac{v^2}{2} + \frac{\gamma}{\gamma - 1}\frac{k_B T}{\mu}\right)\right] = E. \tag{4}$$

In the above equations, v is the common velocity for all fluids and k_B is the Boltzmann constant. ρ, T, γ, and μ are respectively the mass density, temperature, adiabatic exponent, and average molecular mass corresponding to each fluid (namely, neutral, ion, and electron). The source terms M, F and E represent the net rate per unit volume for the generation of mass, momentum, and energy, respectively for each fluid. We also have $\sum_{n,i,e} M = \sum_{n,i,e} F = 0$ (subscripts n, i and e respectively denote the neutral, ion and electron fluids). We define G as the net rate of generation of thermal energy per unit volume for each fluid; we have $G_k = E_k - F_k v + \frac{1}{2} M_k v^2$, where $k \in \{n, i, e\}$. The components G_k for each fluid are calculated as described in Ahmed and Acharyya (2021). The set of Eqs. (1)–(4) can be written as first-order differential equations which we numerically integrate for different gas production rates Q.

2.1. Calculation of ionization rates

Photoionization due to the solar UV flux is a significant driver of the cometary ionospheric population. The UV radiation field does not remain constant throughout the coma; absorption of the UV photons by the cometary neutrals and scattering by nanograins in the coma leads to the attenuation of the UV flux, thus altering the rates of photochemical reactions at different cometocentric distances. The Beer–Lambert law

can be used to derive the flux $\phi(\lambda, r)$ at any cometocentric distance r and wavelength λ:

$$\phi(\lambda, r) = \phi(\lambda, r_\infty) e^{-\tau(\lambda, r)}. \quad (5)$$

$\phi(\lambda, r_\infty)$ is the spectral flux reaching the top of the coma, and the quantity in the exponential is the optical depth, such that:

$$\tau(\lambda, r) = \sum_i \sigma_{i,\mathrm{tot}}(\lambda) \int_r^\infty n_i(r') dr'. \quad (6)$$

In the above expression, $n_i(r')$ is the number density of a neutral cometary species i that is present along the trajectory of the photon at a radial distance r', and $\sigma_{i,\mathrm{tot}}(\lambda)$ is its total photo-absorption cross section at wavelength λ. This expression is valid for the one-dimensional case, i.e., when the spacecraft is along the sun-comet axis. Since that is not usually the case, the radial distance is written as $r = \left(x^2 + y^2 + z^2\right)^{1/2}$, where x is along the sun-comet vector and (y, z) depends on the position of the spacecraft. Eq. (6) is modified as follows:

$$\tau(\lambda, r) = \sum_i \sigma_{i,\mathrm{tot}}(\lambda) \int_{x_0}^\infty n_i \left(\sqrt{x^2 + y_0^2 + z_0^2} \right) dx, \quad (7)$$

where (x_0, y_0, z_0) is the position vector of the spacecraft. The photochemical reaction rate $k(\lambda, r)$ of the species i in the wavelength bin λ and $\lambda + \Delta\lambda$ is:

$$k(\lambda, r) = \sigma_{i,\mathrm{br}}(\Delta\lambda) \Phi(\Delta\lambda, r). \quad (8)$$

where $\sigma_{i,\mathrm{br}}(\Delta\lambda)$ is the wavelength-averaged partial photo-absorption cross section in the wavelength bin and $\Phi(\Delta\lambda, r)$ is the spectral photon flux obtained from Eq. (5) and integrated over $\Delta\lambda$. We sum over all the wavelength bins to get the total rate coefficient (s^{-1}) for the photochemical reaction at a cometocentric distance r.

We have used the wavelength-dependent photo-absorption cross sections contained in the Photo Ionization/Dissociation Rates (PHIDRATES) database, available at phidrates.space.swri.edu. This database is compiled from cross sections given by Huebner and Carpenter (1979), Huebner et al. (1992) and Huebner and Mukherjee (2015). There is no instrument on board *Rosetta* for directly measuring the solar UV flux. Johansson et al. (2017) extracted the photoelectron saturation current from the RPC Langmuir probe measurements, which can be used as an index of the solar far and extreme ultraviolet at the location of *Rosetta*. During the early and late mission phase of *Rosetta*, this data set is well correlated with the UV observations by TIMED/SEE and MAVEN/EUVM, though there is a decrease in the expected photoelectron current near perihelion. The effect of this decrease on our model results is discussed further in Section 4. In the present case, for the solar spectral UV photon flux data, we rely on the wavelength-dependent solar irradiance data set that is available with the Laboratory for Atmospheric and Space Physics Interactive Solar Irradiance Data Center (lasp.colorado.edu/lisird). The spectral fluxes that we have used are derived from the FISM2 (0.1–190 nm) and NRLSSI2 (>190 nm) models. FISM2 (Chamberlin et al., 2020) is an empirical model that is based on data from SORCE/XPS (Woods et al., 2005), SORCE/SOLSTICE (Rottman, 2005), and SDO/EVE (Woods et al., 2012) while NRLSSI2 makes use of the solar irradiance measurements obtained by SORCE (Harder et al., 2005; Kopp et al., 2005; Rottman, 2005). The spectral fluxes given by FISM2 and NRLSSI2 are available at 1 au, and in order to scale them to some other heliocentric distance r_h, we have used the multiplicative factor r_h^{-2}, where r_h is in units of au.

The ionization and dissociative ionization of neutral species also occur due to collisions with energetic electrons present in the coma. To calculate the ionization frequencies, we assume a Maxwellian distribution of the electrons. At an electron temperature T_e, this distribution is written as:

$$f(v) = [m_e/2\pi k_B T_e]^{3/2} \exp\{-m_e v^2/2k_B T_e\}, \quad (9)$$

where m_e is the electron mass and k_B is the Boltzmann constant. The ionization frequency R_{ik} (s^{-1}) for a species i attaining an ionized state k can be calculated as:

$$R_{ik} = n_e \int_{v_{ik}}^\infty v \sigma_{ik}(v) f(v) 4\pi v^2 dv, \quad (10)$$

where n_e is the electron number density, v_{ik} is the velocity corresponding to the ionization potential I_{ik} and σ_{ik} is the cross section. The compiled cross sectional data for the electron impact ionization of various neutral species is available in the literature. These include cross sections for the ionization of the main cometary volatiles namely H_2O (Itikawa and Mason, 2005), CO_2 (Itikawa, 2002) and CO (Itikawa, 2015), as well as for other cometary neutrals namely N_2 (Itikawa, 2006), O_2 (Itikawa, 2009), H_2 (Yoon et al., 2008), and CH_4 (Song et al., 2015). We use these cross sectional data to calculate the electron impact ionization rates from Eq. (10). Modeling of the instrument response of *Rosetta*'s RPC-MIP shows the presence of two electron populations that follow a double Maxwellian electron velocity distribution function (Gilet et al., 2017; Wattieaux et al., 2019). These two populations are hot electrons of energy 5–15 eV and cold electrons of energy 0.1–1 eV. The cold electron population does not possess sufficient energy to ionize neutral molecules (ionization threshold energy of cometary neutrals is >12 eV). Thus, calculating the ionization frequency using a single Maxwellian distribution for the electrons is an acceptable approximation.

3. Dataset

3.1. The Rosetta Plasma Consortium

The five sensors on the Rosetta Plasma Consortium (RPC) are the Ion and Electron Sensor (IES; Burch et al., 2007), the Ion Composition Analyzer (ICA; Nilsson et al., 2007), the Langmuir Probe (LAP; Eriksson et al., 2007), the Mutual Impedance Probe (MIP; Trotignon et al., 2007) and the Magnetometer (MAG; Glassmeier et al., 2007). IES, ICA, LAP, and MIP provide measurements of the plasma number density and each instrument probes different plasma populations (e.g., cold/warm electrons, energetic electrons, cometary ions) associated with different energy ranges. RPC-IES is an electrostatic analyzer designed to measure the ion and electron flux over the energy range from 4.32 eV q^{-1} to 17.67 keV q^{-1}. RPC-ICA is an ion spectrometer that scans the energy and angular space to detect ions of different masses. Its operational energy range is a few eV q^{-1} up to 40 keV q^{-1} and it can distinguish between H^+, He^+, He^{2+} and heavy cometary ions of mass corresponding to water group ions and above.

The RPC-ICA number density measurements are best in low-density plasmas such as solar wind or cometary ions at large cometocentric distances. A limitation of this sensor is that the negative spacecraft potential complicates the observations of ions with low energies. Generally, only a fraction of the low-energy ions are seen by ICA, and the cometary ion density estimates are lower than those from LAP and MIP. There is a net anti-sunward flow of cometary ions (Nilsson et al., 2015, 2017; Berčič et al., 2018), and ICA mainly observes the accelerated ions while the more locally produced plasma is below the threshold energy level of ICA. The negative spacecraft potential affects the detection capability of RPC-IES as well, since low energy electrons cannot reach the sensor, and the electron number density is underestimated. In this work, we use the plasma densities measured from RPC-LAP and RPC-MIP; these are described in the following section.

3.2. Plasma density from LAP and MIP

RPC-LAP consists of two spherical Langmuir probes mounted at the tips of two solid booms that protrude non-symmetrically from the spacecraft (Eriksson et al., 2007). A standard mode of operation of the Langmuir probe is the bias voltage sweep. During a sweep, the probe

bias voltage with respect to the spacecraft is stepped through a series of values, and the current collected by the probe is measured. The current flowing in the probe is proportional to the plasma density and also depends on other factors such as the plasma energy distribution, the applied bias voltage, and the spacecraft potential. The total probe current can be separated into three parts, namely ion, electron, and secondary electron emission currents (Eriksson et al., 2017; Johansson et al., 2017). Electrons dominate the collected current when the probe is at a positive potential with respect to the plasma and the electron number density can be determined from this part of the probe current. When the potential is negative, positively charged ions are collected. In a tenuous and sunlit plasma, the photoelectrons emitted from the probe dominate the collected current, which can be used to estimate the integrated solar UV flux (Johansson et al., 2017).

RPC-MIP is an active electric sensor that measures the transfer impedance between a transmitting monopole or dipole and a receiving dipole (Trotignon et al., 2007). The instrument offers different time resolutions and operates within different frequency bands in the 7–3500 kHz range. There are two modes of operation, namely the passive mode in which the transmitters are off, and the active mode in which the transmitters stimulate the surrounding plasma. When operating in the active mode, the electrodes on the RPC-MIP can be used independently or cojointly as monopole or dipole transmitters, respectively. This is known as the SDL (Short Debye Length) mode, while in the LDL (Long Debye Length) mode, the LAP2 probe of RPC-LAP serves as the monopole transmitter. The LDL mode, while preventing RPC-LAP from being fully operational, enables the measurement of plasma of lower density than that measured in the SDL mode since plasma at larger spatial distances from the receivers is triggered. Since charge neutrality is maintained, the ion density in the plasma can be estimated from the electron density. RPC-MIP measures the electron density by identifying the plasma resonance frequency f_p in the mutual impedance spectrum, i.e., the response of the plasma to a weak transmitted electric signal. f_p is only dependent on the number density and thus, MIP can provide accurate density estimates within its operational range. Due to instrumental limitations, RPC-MIP can measure the electron density in the range of $10 - 10^5$ cm^{-3} for energy (eV) <0.05 n_e in the SDL mode and 1–350 cm^{-3} for energy (eV) <0.15 n_e in the LDL mode.

If the electron density is too low in the SDL mode of RPC-MIP, the density can be retrieved from the LDL mode, though the LDL mode has its limitations as well. If the Debye length is too high (for low electron density), the instrument becomes blind to the plasma. On the other hand, if the plasma frequency is higher than the detectable limit (for high electron density), saturation is reached in the measured density (Heritier et al., 2018). The dataset obtained by the cross-calibration of the measurements of RPC-LAP and RPC-MIP overcomes these operational limitations and is available in ESA's Planetary Science Archive (Besse et al., 2018). The recommended dataset for long-term studies is the low time resolution LAP/MIP cross-calibrated data product known as NED, available as ned.tab files in the LAP derived data folder in PSA. This dataset has a time resolution varying between 32 s and a few minutes, a high dynamic range, and the broadest coverage over the mission period, and its homogeneous nature makes it suitable for statistical studies. The accuracy of an individual data point is less than the MIP density, but the wide dynamic range ensures lesser systematic bias towards high or low densities.

3.3. Neutral density from ROSINA

The ROSINA-COPS pressure sensor consists of two gauges, namely the nude gauge that measures the total density of the cometary gas at the spacecraft location and the ram gauge that measures the ram pressure which is equivalent to the gas flux. The COPS operating principle is that the gas is ionized by electron impact and the resulting ion current is measured. The instrument sensitivity to the different gas species is not the same due to differences in the electron impact ionization cross sections and correction factors are required for the individual species. The relative abundances of the species in the gas, available from the DFMS and RTOF measurements, are required to calculate the weighted average of the ionization cross section and the absolute abundances of the species (Gasc et al., 2017). The level 4 ROSINA density data in PSA is the corrected data that represents the actual neutral density of the coma.

Läuter et al. (2020) considered the period from 1 August 2014 (377 days before perihelion) to 5 September 2016 (390 days after perihelion) and divided this period into 50 time intervals of length varying between 7 to 29 days. The intervals I_{1-50} were chosen in a way that the sub-spacecraft position samples sublimation from nearly all the surface elements of 67P/C-G, but there is limited variation in the heliocentric distance and subsolar latitude within the interval. For each of these intervals, Läuter et al. (2020) used the combined DFMS and COPS measurements to derive the temporal evolution of the production rates of 14 volatile species belonging to the set S where

$$S = \{\mathrm{H_2O}, \mathrm{CO_2}, \mathrm{CO}, \mathrm{H_2S}, \mathrm{O_2}, \mathrm{C_2H_6}, \mathrm{CH_3OH}, \mathrm{H_2CO}, \mathrm{CH_4}, \mathrm{NH_3}, \mathrm{HCN}, \mathrm{C_2H_5OH}, \mathrm{OCS}, \mathrm{CS_2}\}. \quad (11)$$

These production rates compare well with other production rate results calculated based on the *Rosetta* instruments VIRTIS (Fougere et al., 2016), MIRO (Marshall et al., 2017; Biver et al., 2019), DFMS (Combi et al., 2020) and COPS (Hansen et al., 2016).

3.4. Model runs

The bottom panel in Fig. 1 shows the time series variation of the COPS neutral density and the LAP/MIP cross-calibrated electron density in the plasma. We use the convention of negative values for indicating days before perihelion. COPS data is unavailable or has large uncertainty during the "safe mode" of operations (1–10 April 2015) and the excursions to large cometocentric distances (dayside excursion in late-September to mid-October 2015 and tail excursion in late-March to early April 2016). The vertical shaded regions in Fig. 1 indicate the time period around the excursions which have been excluded in the analysis by Läuter et al. (2020); the time period of the safe mode was included in I_{1-50}.

The comet surface can be treated as a mesh of triangular faces, each of which is treated as a source of volatile emission. The neutral gas density at the spacecraft location is the result of the superposition of gas expansion from these emission sources (Kramer et al., 2017; Läuter et al., 2019). Considering gas emission only from the surface (though subsurface sublimation may also occur), Läuter et al. (2020) retrieved the surface emissions using a mesh of 3996 triangular faces given by Preusker et al. (2017). The time series of the retrieved production rates by Läuter et al. (2020) for all 14 volatiles in set S is available as ancillary files to arxiv.org/abs/2006.01750. We have used these production rates as inputs in our model runs.

4. Results

We present our model results for the intervals in which the heliocentric distance $r_h < 3$ au (time intervals I_7 to I_{42} as defined by Läuter et al. (2020)). At large heliocentric distances, particularly when $r_h > 3$ au, the outgassing rate is weak. Ions that are created due to the ionization of neutral species suffer only a limited number of collisions as the mean free path is larger at low densities, and the advection timescale is smaller than the chemical timescale (Beth et al., 2016). In each time interval, we have used our chemical-hydrodynamical model and obtained numerical solutions to Eq. (1) to get the variation of the ion density with cometocentric distance.

Due to limited surface coverage of the spacecraft, some of the surface elements do not have production rates assigned to them. To constrain the production rates from these elements, Läuter et al. (2020)

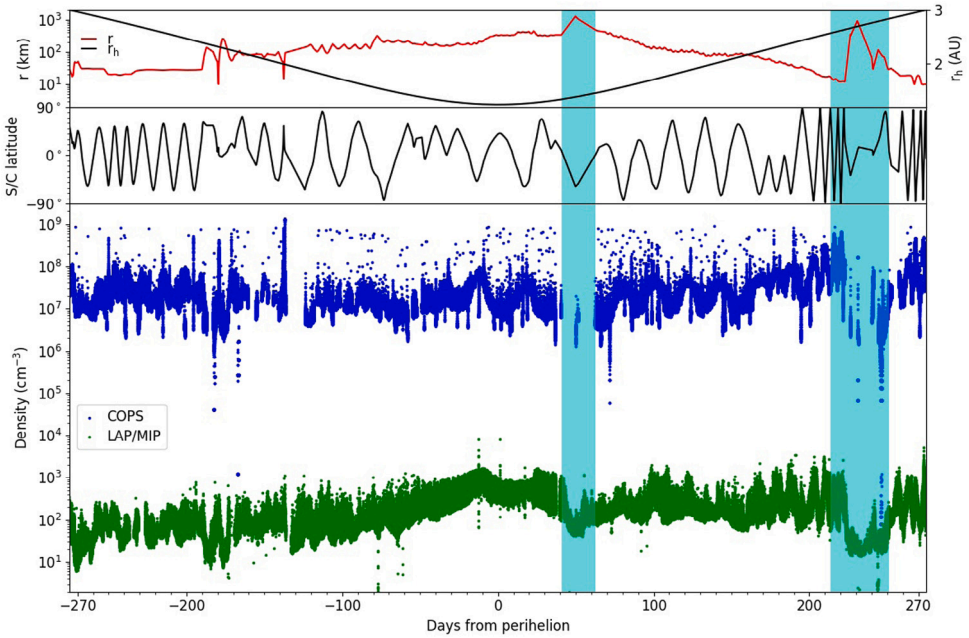

Fig. 1. Top panel: time series of the cometocentric distance of *Rosetta* (red line, left y-axis) and the heliocentric distance of 67P/C-G (black line, right y-axis). Middle panel: time series of the sub-spacecraft latitude. Bottom panel: time series of the neutral density measured by COPS (blue pixels) and the cross-calibrated electron density from LAP/MIP (green pixels). The shaded vertical regions indicate the time period around the dayside and tail excursions. (For interpretation of the references to color in this figure legend, the reader is referred to the web version of this article.)

have given upper and lower limits in their derived time series global production rates. The lower limit is set by assigning zero to the emission from the unknown surface element. The upper limit in the time interval I_j is set by assigning the maximum production from that surface in the neighboring time intervals I_{j-1} and I_{j+1}. Thus, in order to better constrain the modeled ion densities, we obtain two sets of model runs for each time interval and the input production rates are set as the upper and lower bounds respectively. We also obtain a third set of models where we take the average of the upper and lower bounds as inputs.

4.1. Total ion density

Figs. 2, 3, and 4 show a comparison of our model obtained ion densities with the LAP/MIP cross-calibrated plasma density for different time intervals $I_j, j = (7, 42)$. The LAP/MIP density data is smoothed by taking a moving average. In a particular time interval I_j, our model runs give the radial variation of the ion number density and we can find the number density at the cometocentric distance that corresponds to the spacecraft location. The model is not able to capture the high frequency density fluctuations in the plasma. The variations in our modeled ion density in the interval I_j result due to changes in the spacecraft distance. We divide the time intervals into three groups in order to assess the trends in the modeled density.

4.1.1. Group 1: Intervals I_7 to I_{15}

The first group includes the intervals I_7 to I_{15} (Fig. 2) and corresponds to the pre-perihelion period where $r_h > 1.8$ au, up to the time when *Rosetta* enters the safe mode. The total outgassing rate Q varies from $\sim 10^{26}$ s^{-1} to $< 10^{27}$ s^{-1}. In the first half of this group, there is limited change in the cometocentric distance and the spacecraft remains roughly at a height of 20–30 km from the surface. In the latter part of this group, r shows variation within a time interval, even becoming more than 100 km. This variation is reflected in the modulation of the ion density in I_{13} and I_{14}, and a peak-like feature in the early part of I_{15}. Since the outgassing rate is low, most of the ions are created at smaller r and a change in the cometocentric distance by 50 km or more is marked by a reduction in the total ion density.

In order to estimate the extent to which our modeled densities deviate from the LAP/MIP observed plasma density, we have calculated the ratio between these two quantities, as shown in the bottom panel of Fig. 2. We see that for the lower bound of the production rate, this ratio remains close to 1. The fluctuations in the ratio are due to the fluctuations in the LAP/MIP density, which cannot be captured in our model as mentioned previously. For the upper bound of Q, the ratio mostly remains between 1–2. In the intervals I_{12} to I_{15}, the ratio for the lower bound of Q varies between 1–2, while the upper bound of Q leads to an overestimation of the ion density by factors of 2–4 (excluding the safe mode).

The interaction of 67P/C-G with corotating interaction regions (CIRs) and coronal mass ejections leads to disruptions in the cometary plasma environment (Edberg et al., 2016a,b; Hajra et al., 2017; Goetz et al., 2019). Of the four CIRs that impacted 67P/C-G from October to December 2014, two of them, namely event 3 and event 4 defined by Edberg et al. (2016b) fall within the intervals I_7 and I_9, respectively. An increase in the observed density towards the end of I_7 corresponds to event 3 while the moderate increase in the density at the start of I_9 indicates the time of event 4. The response of the cometary plasma to individual events is variable, though these effects are not included in our model.

4.1.2. Group 2: Intervals I_{16} to I_{31}

The second group consists of the intervals I_{16} to I_{31} and the corresponding densities are shown in Fig. 3. This group includes the time intervals corresponding to the inbound leg from 1.8 au of the journey of 67P/C-G on its orbit around the Sun, the perihelion crossing at $r_h = 1.24$ au, and the outbound journey post-perihelion up to 1.8 au. The spacecraft distance from the comet varies between 100–400 km and the production rate ranges between 10^{27} s^{-1} $< Q <$ 10^{29} s^{-1}. In the intervals $I_{16} - I_{18}$, there is some modulation in the modeled ion density due to changes in r, while the density remains nearly constant in other intervals. The intervals near perihelion, characterized by high outgassing rates, exhibit ion densities exceeding 1000 cm^{-3}, even though $r > 200$ km. The production rate calculated by Läuter et al. (2020) peaks in I_{25} and we find that the total ion density is also maximum in this interval.

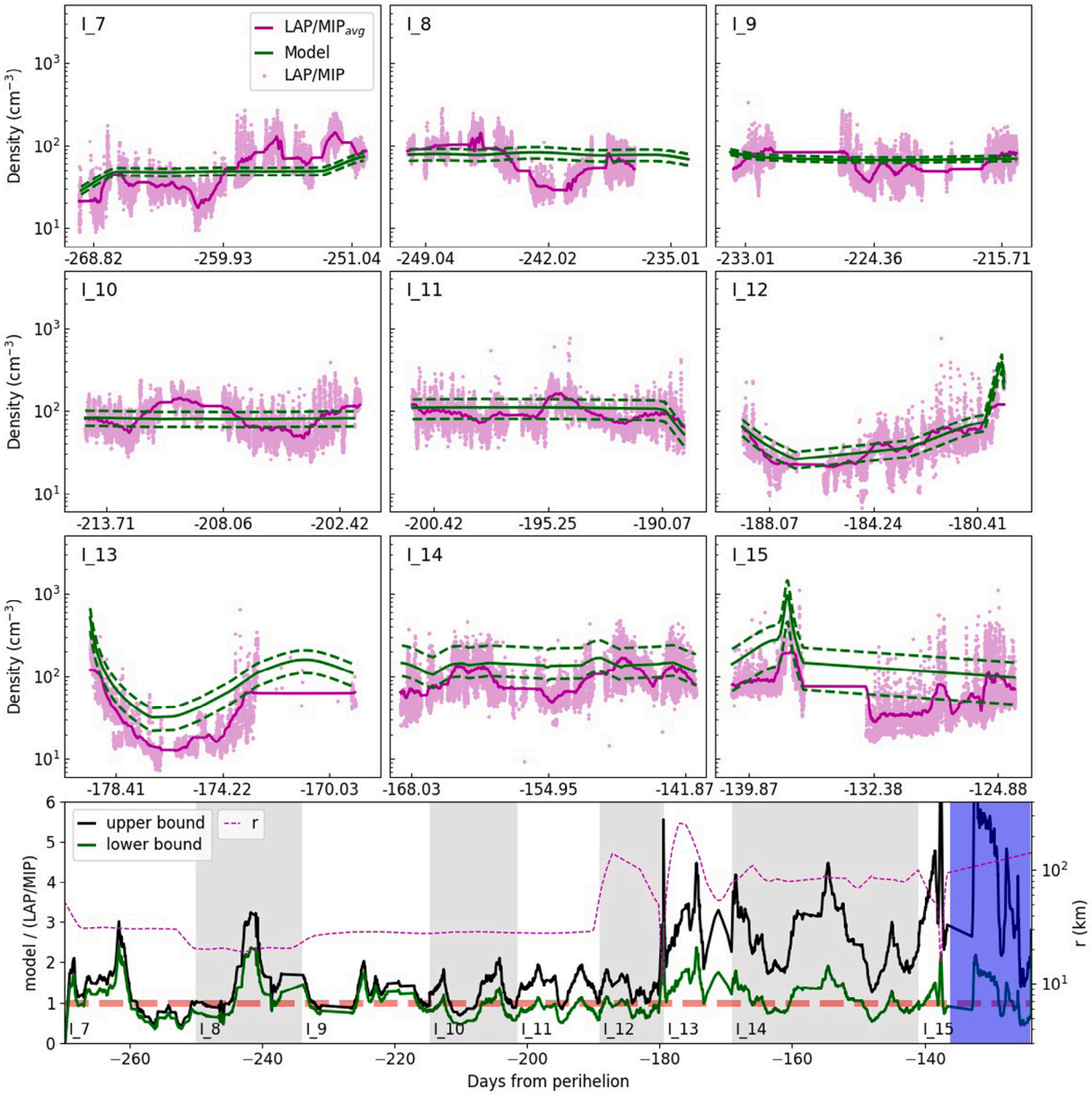

Fig. 2. Subpanels in the top 3 rows: time series of the plasma density at the spacecraft location for the intervals I_7 to I_{15}. The pink pixels show the instantaneous LAP/MIP cross-calibrated density while the pink lines show the smoothed density obtained by taking a moving average. The green lines show the total ion density obtained from our models for the upper and lower bounds of the production rate (dashed lines) and the average of the upper and lower bounds (solid lines). Bottom panel: ratio between the modeled total ion density and the LAP/MIP plasma density for the upper (black line) and lower (green line) bounds of the production rate. The ratio is 1 on the dashed horizontal line. The intervals I_7 to I_{15} are indicated by the white (odd-numbered intervals) and gray (even-numbered intervals) regions. The blue vertical shaded region indicates that the spacecraft was in the safe mode. The pink dashed line is the spacecraft distance from the nucleus (scale: right y-axis). (For interpretation of the references to color in this figure legend, the reader is referred to the web version of this article.)

Johansson et al. (2017) used measurements from TIMED/SEE at Earth and MAVEN/EUVM at Mars for epochs when these two planets were at the same solar longitude as *Rosetta* in order to estimate the flux propagated out to the comet location. They find that the photoemission current derived from TIMED/SEE and MAVEN/EUVM correlate well with the photoemission current obtained from the RPC-LAP measurements at 67P/C-G. They also find that around perihelion, the photoemission current from RPC-LAP reduces to nearly half of the expected value as estimated from MAVEN/EUVM, due to attenuation of the UV flux. As described in Section 2.1, our model includes the effect of the extinction of UV due to photo-absorption by the coma gas, though we do not find any appreciable change in the UV flux at the location of the spacecraft. Johansson et al. (2017) calculate the EUV absorption by water molecules to be only $0.8 \pm 0.1\%$ near perihelion, at a cometocentric distance of 330 km. Heritier et al. (2018) also note that during the entire escort phase, there is no significant change in the plasma density due to photo-absorption. Johansson et al. (2017) propose scattering and absorption by cometary dust grains as a possible reason for the reduction in the photoemission current. Thus, we also ran models where we reduced the photoionization rate by half, and the resulting total ion densities are indicated by the blue dashed lines in the subpanels of Fig. 3. The total ion density at the reduced photoionization rate is closer to the LAP/MIP observed total plasma densities (Fig. 3, bottom panel). The ion ratio varies between 1–2 for the lower bound of Q, and between 1–3 for the upper bound. However, in I_{18}, the ratio reaches a high value, even at the reduced photoionization rate. Nemeth (2020) finds that variations in the external solar wind pressure induce movements in the diamagnetic cavity boundary. For an inward

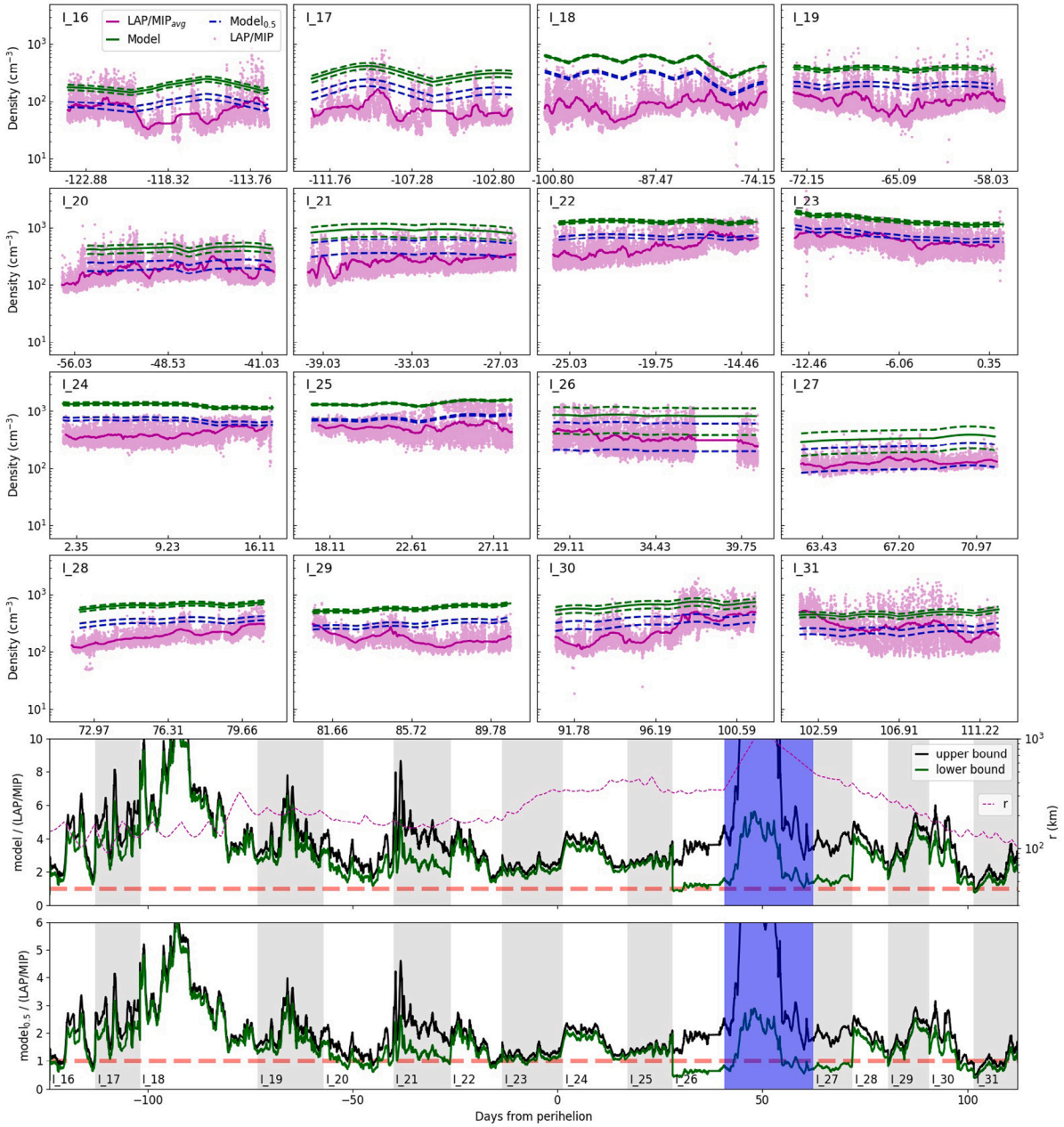

Fig. 3. Same as Fig. 2 but for the time intervals I_{16} to I_{31} and the following modifications: the blue dashed lines in the subpanels show the ion density for the upper and lower bounds of the production rate when the photoionization rate is reduced by 50%. Of the two bottom panels, the upper one shows the density ratio described in the caption of Fig. 2 while the lower one shows the density ratio at the reduced photoionization rate. The blue vertical shaded regions in the two lower panels indicate the dayside excursion. (For interpretation of the references to color in this figure legend, the reader is referred to the web version of this article.)

moving boundary, the plasma density and suprathermal ion counts increase rapidly. Conversely, when the boundary moves outward, these quantities decrease, but more gradually. Thus, the decrease in the observed plasma density in I_{18} (resulting in an increased model to LAP/MIP ion ratio) could be due to this effect. The observed plasma density modulations due to solar wind pressure changes may also be present in the other intervals near perihelion ($I_{16} - I_{21}$).

4.1.3. Group 3: Intervals I_{32} to I_{42}

The third group (Fig. 4) includes the intervals I_{32} to I_{42} where the heliocentric distance is >1.8 au and <3 au. The spacecraft distance remains below 100 km, except during the tail excursion (not included in our model runs). The outgassing rate is $\sim 10^{27}$ s^{-1} in the first half of the group, while it goes below 10^{26} s^{-1} in the last few intervals. The decrease of H_2O outgassing post-perihelion is steeper than its increase pre-perihelion (Läuter et al., 2020). This is in contrast to volatiles such as CO and CO_2, which show a slower decay at $r_h > 2.4$ au. Thus, there is a marked increase in the relative abundance of volatiles with respect to water; in fact, $Q_{CO_2} > Q_{H_2O}$ in the interval I_{42}.

The ion ratios mostly vary between 2–3 in the first half of this group. This corresponds to the period of December 2015 to late January 2016, for which Johansson et al. (2017) calculated the photoionization rates to be reduced by a factor of ~0.6. From Fig. 3, we see that a reduction in the photoionization rate by a factor of 0.5 leads to a reduction in the ion density by approximately the same amount. By applying a reduction of a factor of 0.6 to the intervals I_{32} to I_{36}, the ion ratio would be within 1–2. I_{41} and I_{42} show oscillation in their LAP/MIP measured density, which is correlated to the latitudinal variation of *Rosetta*, and the ion

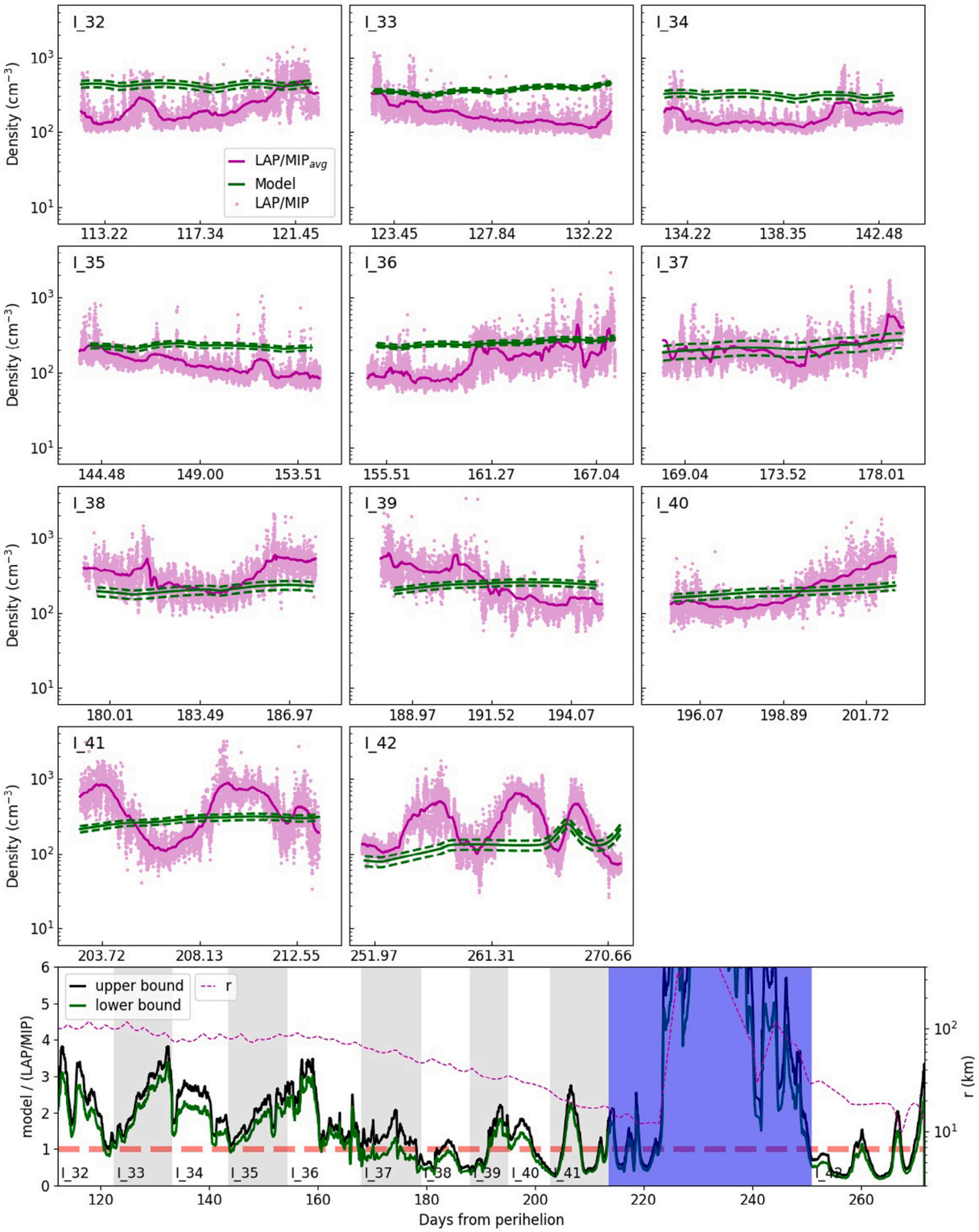

Fig. 4. Same as Fig. 2 but for the time intervals I_{32} to I_{42}. The blue vertical shaded region in the bottom panel indicates the tail excursion.

ratio shows a similar oscillation. Nemeth et al. (2020) defined a simple distance, latitude, and longitude dependent first order cosine function to model the 3D spatial distribution of the cometary plasma. This model was able to reproduce quite well the plasma density distribution in the last month of *Rosetta*'s operations. The features in I_{41} and I_{42} can probably be similarly explained. In I_{42}, the spacecraft is very close to the nucleus, the production rate is low, and our model underestimates the total ion density.

4.2. Density of major ions

In this section, we discuss the densities of some of the primary ions that form in the coma due to gas phase chemistry, as obtained

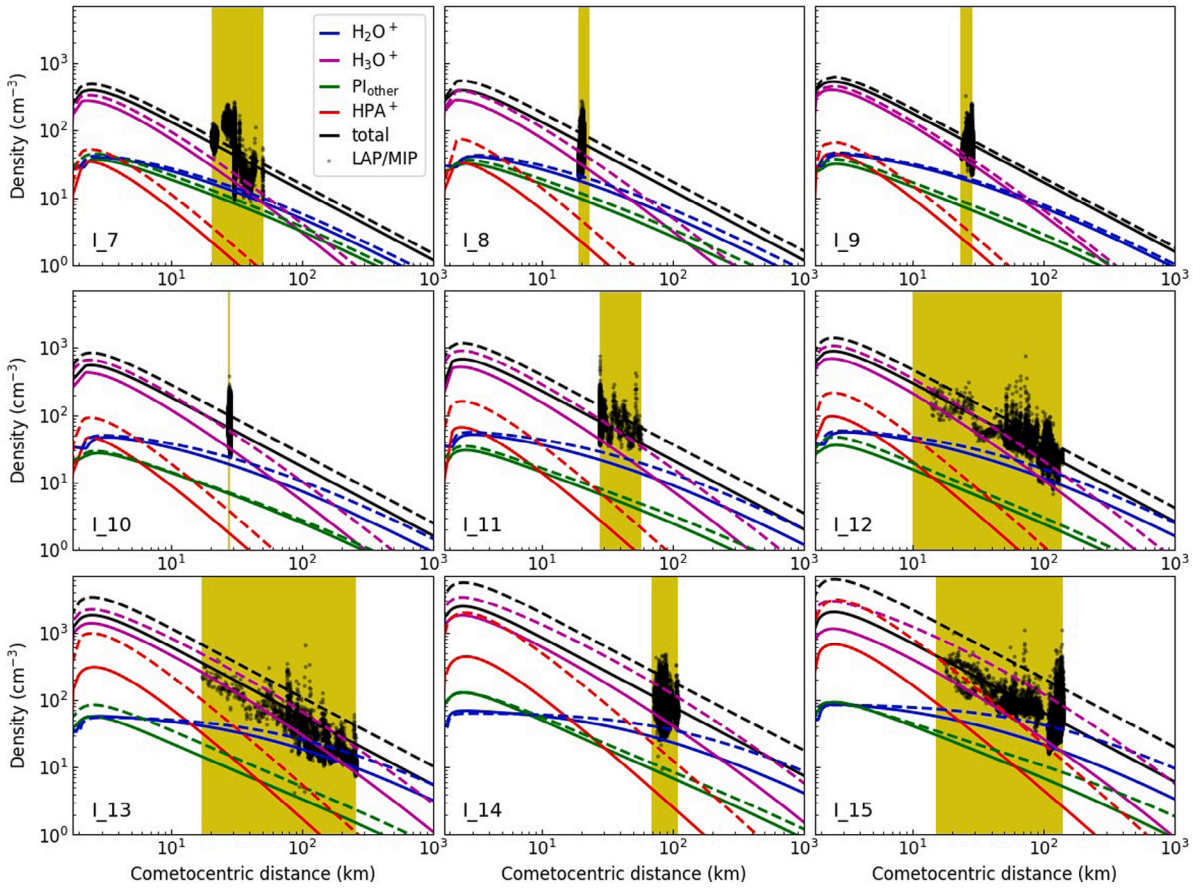

Fig. 5. The subpanels show the variation of the total plasma density and the densities of H_2O^+, H_3O^+, HPA^+, and PI_{other} ions with cometocentric distance for the time intervals I_7 to I_{15}. The solid lines and dashed lines denote the lower and upper bounds, respectively. The black pixels show the LAP/MIP density and the yellow vertical shaded regions in each subpanel denote the variation of the cometocentric distance of *Rosetta* within the interval.

from our model runs. The ions that we consider are H_2O^+, H_3O^+, and the two ion groups labeled HPA^+ and PI_{other} in Figs. 5–7. H_2O^+ ions are created by the ionization of water molecules, which further react with H_2O to form H_3O^+ ions. It is well known that in the coma, a neutral species A that has a proton affinity higher than water undergoes protonation by reacting with H_3O^+ ions to form $A{-}H^+$ ions (see, for example, Vigren and Galand (2013) and Heritier et al. (2017a)). From the parent neutrals in set S, we identify a subset that consists of these high proton affinity (HPA) neutrals, such that HPA = {NH_3, CH_3OH, HCN, H_2CO, H_2S and C_2H_5OH}. We define HPA^+ as the sum of the ions (NH_4^+, $CH_3OH_2^+$, and so on) formed by the protonation of the HPA neutrals. Since NH_3 has the highest proton affinity, the terminal ion in the protonation chain is NH_4^+, and NH_3 will also accept H^+ ions from other protonated species, such as $CH_3OH_2^+$ and H_3S^+. In general, a neutral species will undergo proton transfer reactions with H_3O^+ as well as other species that lie below it on the proton affinity ladder. Finally, PI_{other} denotes the sum of the ionized parent species of set S excluding H_2O, namely the sum of the ions CO_2^+, CO^+, and so on. The cometocentric distance variation of H_2O^+, H_3O^+, HPA^+ and PI_{other} is shown in Figs. 5–7 for each of the intervals $I_j, j = (7, 42)$. The yellow-shaded regions show the extent of the change in the cometocentric distance of *Rosetta* within each interval, indicating that the model estimated density of the ions lies within that region.

Following the same grouping of time intervals as described in the previous section, we see that in the first half of the group 1 intervals, H_3O^+ is the most abundant ion at the spacecraft location, followed by H_2O^+. Since the coma density is low, HPA^+ ions may form close to the nucleus surface, though their density decreases rapidly, such that at the spacecraft location, the density $\lesssim 2$ cm^{-3}, which is less than what we estimate for H_2O^+ and PI_{other} ions. As the comet moves closer to perihelion and there is an increase in the production rate, the density of HPA^+ ions increases and may even become more than that of H_2O^+ for certain spacecraft locations. The density of PI_{other} remains less than that of H_2O^+ at the spacecraft location since the sum of parent volatiles other than water makes up about 10–15% of the total gas production. Out of these, the most dominant volatiles are CO_2, CO and O_2, hence the main contributing ions are CO_2^+, CO^+ and O_2^+. Apart from ionization, parent species also undergo dissociative ionization to produce ion fragments, for example, the dissociative ionization of CH_4 creates CH_3^+, CH_2^+ and CH^+ ions, and NH_3 produces NH_2^+ and NH^+ ions. However, we do not consider these fragment ions in the present case, since their contribution to the total ion density at the spacecraft location is generally orders of magnitude lower than H_2O^+ (Beth et al., 2020).

For the group 2 time intervals (Fig. 6), the radial variation of the number density of H_2O^+ is relatively weaker than the group 1 intervals. The loss of H_2O^+ due to ion-neutral reactions is nearly equal to its rate of creation by ionization, causing it to remain in photochemical equilibrium. The increased outgassing rate drives more active chemistry and the HPA^+ ions dominate over H_3O^+ at low cometocentric distances. As the cometocentric distance increases, the decrease in the coma density reduces the rate of collisions for chemical reactions to occur. Since the H_2O^+ density remains nearly constant, the decrease in the production of H_3O^+ is proportional to the decrease in the neutral density of its parent species (water). On the other hand, the decrease in the production of HPA^+ (for example, NH_4^+) is proportional to the decrease in the density of the parent HPA (NH_3 in this example) as well as the decrease in the density of the ion from which it accepts H^+

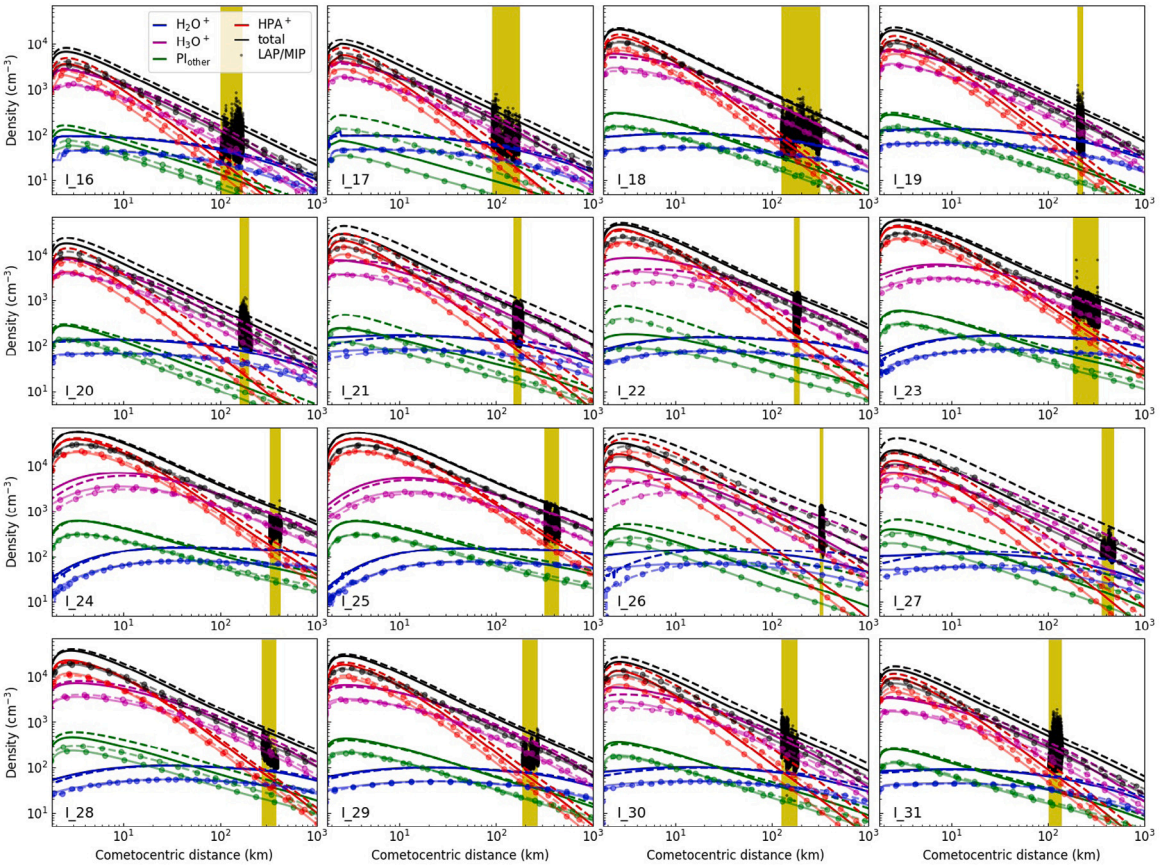

Fig. 6. Same as Fig. 5 but for the time intervals I_{16} to I_{31}. Additionally, the lines with circular markers denote the ion densities when the photoionization rate is reduced by 50%.

(for example, H_3O^+). This causes H_3O^+ to be the dominant ion at the spacecraft location. The main contributing ions to PI_{other} are O_2^+ and CH_3OH^+, with a smaller contribution from CO_2^+. At low distances, the density of PI_{other} is higher than that of H_2O^+. This is because H_2O^+ is destroyed rapidly due to collisions with H_2O while O_2^+ and CH_3OH^+ do not react with H_2O. Although CO has a relative abundance higher than most other trace volatiles, it reacts with H_2O via ion-neutral and charge exchange reactions, and it does not contribute significantly to PI_{other}.

In the first half of the group 3 time intervals (Fig. 7), the ion composition shows similarities with the group 2 intervals, with H_3O^+ dominating at the spacecraft location, while at low cometocentric distances, HPA^+ and PI_{other} show densities that are higher than H_3O^+ and H_2O^+, respectively. In fact, this is the trend followed in the intervals in which $Q > 10^{27}$ s^{-1}. In the latter half, the density of HPA^+ ions at low cometocentric distances is nearly equal to H_3O^+, which is different from what we see for the pre-perihelion case of the group 1 intervals. This can be explained by the sharper decline in the H_2O sublimation rate post-perihelion, which results in a higher relative abundance of the HPA neutrals and a higher density of HPA^+. The same is true for PI_{other} ions that show a higher density than H_2O^+ for low cometocentric distances. In this case, CO_2^+ is the dominant ion contributing to PI_{other} at the spacecraft location while most of the other ions show number densities of ~0.5–3 cm^{-3}. We have not shown the ion composition for the intervals I_{41} and I_{42} in Fig. 7; for these intervals, the low spacecraft distance and the latitudinal variability lead to high uncertainties in modeling the coma chemistry.

The total ion densities shown in Figs. 5–7 follow a near power law radial dependence. We derived the power law of the total plasma number density n_{tot} at the cometocentric distance r as

$$n_{tot} = c_2 r^{c_1}. \quad (12)$$

Table 1 shows the values of the fitted parameters c_1 and c_2 for the lower and upper bounds of the modeled number density in different time intervals. The ion density for most intervals varies approximately as r^{-1} which is expected. However, for intervals near perihelion, when ion-neutral reaction rates are faster, there is a deviation from the r^{-1} dependence.

5. Discussions

Following the in situ detections of a large number of ions by *Giotto* at 1P/Halley, Haider and Bhardwaj (2005) showed that photochemical modeling can be used to estimate the densities of the detected ion peaks in the mass spectra. In anticipation of the *Rosetta* observations near perihelion, Vigren and Galand (2013) predicted the ion composition of 67P/C-G by assuming the neutral composition to be made up of H_2O, CO and 1% of high proton affinity neutrals. Heritier et al. (2017a) improved the number density estimates for the near perihelion conditions using neutral measurements from ROSINA-COPS. In some studies, the ratios between the integrated ion counts of two ion species, such as NH_4^+/H_2O^+, NH_4^+/H_3O^+ and H_3O^+/H_2O^+ were used to estimate the ion densities in the coma (Beth et al., 2016; Fuselier et al., 2015, 2016). However, as pointed out by Heritier et al. (2017a), a problem with this approach is that the DFMS scans for two ions are not simultaneous. Additionally, only a small part of the full ion distribution is sampled due to the narrow DFMS field of view and the inability of ions of all energies to pass through the DFMS electrostatic analyzer.

From the results that we have presented in the previous section, we see that our photochemical model can provide an estimate towards the cometary ionospheric composition within factors of 1–3 for the group 1 intervals and 2–3 for the group 3 intervals. For the group 2 intervals, if we include UV extinction, the ion density is estimated within factors of 1–4, though it is overestimated by up to a factor of 6 in the interval

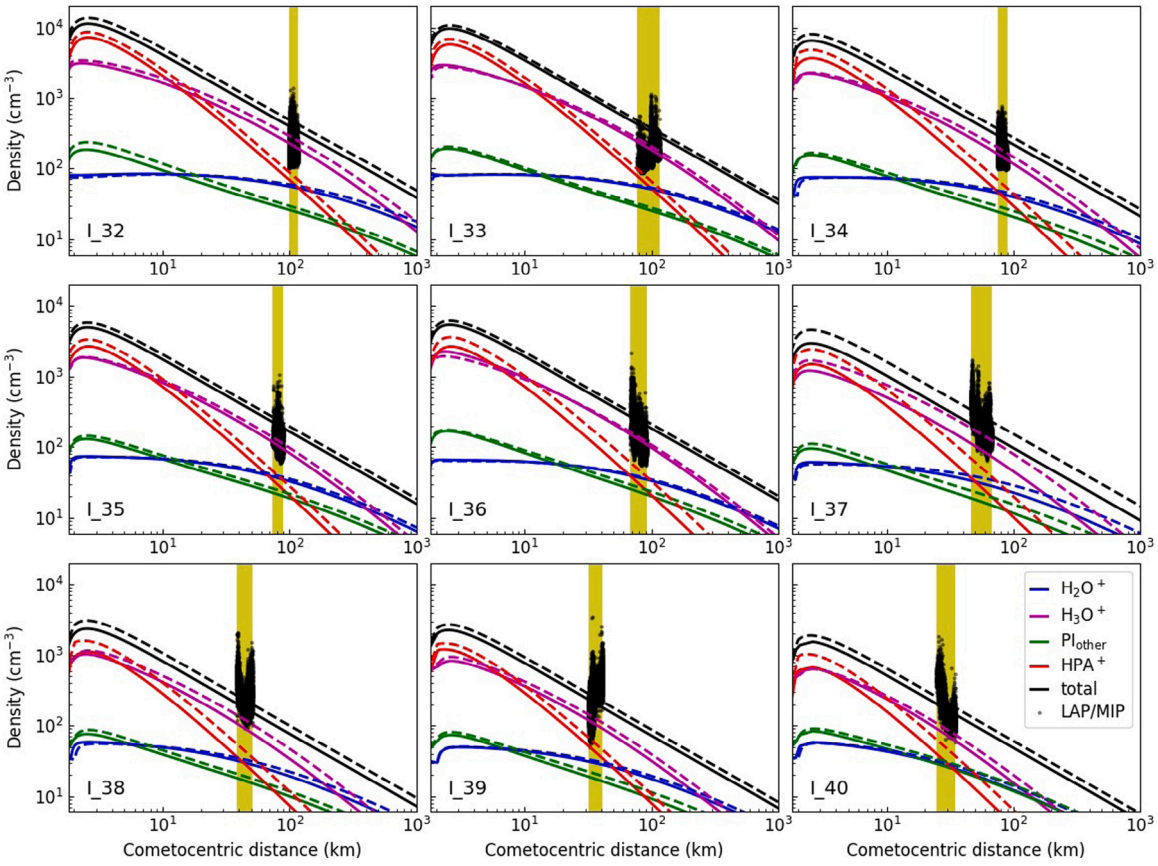

Fig. 7. Same as Fig. 5 but for the time intervals I_{32} to I_{40}.

I_{18}. Additionally, if we consider the lower bound of the production rates provided by Läuter et al. (2020), the modeled ion densities are closer to the observed densities, as compared to the upper bound. Our model runs show that for most of the time intervals in our study, H_3O^+ has the highest density at the location of *Rosetta*, followed by H_2O^+. The density of the HPA^+ ion group at the spacecraft location is generally lower than that of H_2O^+, though around perihelion, it becomes similar to or even larger than H_2O^+. The ions belonging to the ion group PI_{other} generally have the least abundance among all the ions considered.

Since most cometary neutrals have ionization threshold energies of 12–14 eV, Goetz et al. (2022) point out that the energy of photoelectrons created in the coma is not sufficient to cause electron impact ionization at high heliocentric distances (>2 au). At these distances, electron impact ionization is likely to be caused by solar wind electrons (∼10 eV) accelerated by the ambipolar electric field. In our models, at high heliocentric distances, the photoionization rates are 2–3 orders of magnitude higher than the electron impact ionization frequency since we only consider impact ionization by photoelectrons. In order to model the impact ionization by solar wind electrons, we would have to include kinetic effects. This is currently beyond the scope of the current work though we aim to incorporate these effects in the future. Galand et al. (2016) show that for some periods (i.e. when the spacecraft is in the northern hemisphere), photoionization alone can explain the ionospheric density, and the inclusion of electron impact ionization leads to an overestimation of the density. In the southern hemisphere, electron impact ionization is required to explain the ion density. Such seasonal variations are also noted by Heritier et al. (2018).

Our assumption of a common bulk velocity for the ions and neutrals works well for low cometary activity and at a distance of several tens of kilometers from the nucleus, as also seen in other studies (for example, Galand et al. 2016, Vigren et al. 2016, Heritier et al. 2017b, 2018). This assumption may not hold when the spacecraft is further away from the nucleus (beyond 100 km) and for the higher outgassing rates near perihelion. Ion velocity measurements near perihelion show values of 2–8 km s^{-1}, as opposed to a neutral outflow velocity of ∼1 km s^{-1} (Vigren et al., 2017). This may be caused by the acceleration of the ions along the ambipolar electric field set up by the electron pressure gradient. Odelstad et al. (2018) find the ion velocity to be distributed around 3.5–4 km s^{-1} inside the diamagnetic cavity and higher velocities of $\lesssim$8–10 km s^{-1} in the surrounding region, indicating that the ion-neutral drag force does not balance the outside magnetic pressure at the cavity boundary. These effects may result in an overestimation of the modeled density by factors of 2–5 (Vigren et al., 2019).

The cometary ion flow patterns are also affected by the solar wind electric fields. Studies have identified two ion populations, namely the pick-up ion population that gains its energy and momentum through interactions with the solar wind upstream of the observation point and the expanding ion population of cometary origin that gains most of its energy in the vicinity of the nucleus (Nilsson et al., 2015, 2017, 2020; Behar et al., 2016; Berčič et al., 2018). While the motion of the former ion population is governed by the solar wind electric field, the latter ion population is accelerated by the ambipolar electric field in the vicinity of the nucleus and its motion is radially away from the comet nucleus in the $Y - Z$ plane perpendicular to the comet-Sun direction. This is in agreement with the strong shielding of the inner coma from the solar wind electric field at sufficiently high activity (Nilsson et al., 2018). Based on observations of anti-sunward streaming cometary ions, it is suggested that there is an anti-sunward component of the electric field that has a strength of about 10% of the solar wind electric field. Although there is an asymmetry in the coma of 67P/C-G, there is not much influence in the flow direction (Berčič et al., 2018). Since most of the cometary ions are created by the ionization of neutrals that expand radially, Edberg et al. (2019) point out that it is reasonable to assume that the cometary plasma originates in the region between *Rosetta* and

Table 1
Parameters used to fit a power law to the total ion density for the lower and upper bounds.

Molecule	Lower bound		Upper bound	
	c_1	c_2	c_1	c_2
I_7	−1.015	1.345e+03	−1.012	1.638e+03
I_8	−1.017	1.344e+03	−1.014	1.814e+03
I_9	−1.014	1.772e+03	−1.013	2.059e+03
I_{10}	−1.015	1.827e+03	−1.012	2.745e+03
I_{11}	−1.011	2.212e+03	−1.010	3.791e+03
I_{12}	−1.012	2.905e+03	−1.008	4.506e+03
I_{13}	−1.005	5.761e+03	−1.003	1.078e+04
I_{14}	−1.003	7.800e+03	−0.995	1.764e+04
I_{15}	−1.007	6.492e+03	−0.994	1.949e+04
I_{16}	−0.999	2.160e+04	−0.995	2.614e+04
I_{17}	−1.002	3.292e+04	−0.987	3.979e+04
I_{18}	−0.965	6.584e+04	−0.961	6.962e+04
I_{19}	−0.975	6.268e+04	−0.968	7.194e+04
I_{20}	−0.982	5.592e+04	−0.966	7.202e+04
I_{21}	−0.969	8.977e+04	−0.937	1.344e+05
I_{22}	−0.925	1.484e+05	−0.919	1.653e+05
I_{23}	−0.896	1.916e+05	−0.882	2.063e+05
I_{24}	−0.878	2.158e+05	−0.856	2.149e+05
I_{25}	−0.853	2.191e+05	−0.840	2.160e+05
I_{26}	−0.952	9.797e+04	−0.879	1.934e+05
I_{27}	−0.975	6.940e+04	−0.930	1.306e+05
I_{28}	−0.932	1.283e+05	−0.920	1.433e+05
I_{29}	−0.944	9.363e+04	−0.940	1.055e+05
I_{30}	−0.960	6.695e+04	−0.949	8.743e+04
I_{31}	−0.980	4.518e+04	−0.972	5.506e+04
I_{32}	−0.984	3.594e+04	−0.980	4.397e+04
I_{33}	−0.988	3.015e+04	−0.987	3.420e+04
I_{34}	−0.996	2.100e+04	−0.995	2.631e+04
I_{35}	−0.998	1.590e+04	−0.998	1.881e+04
I_{36}	−0.993	1.712e+04	−0.992	1.973e+04
I_{37}	−1.004	9.549e+03	−1.000	1.490e+04
I_{38}	−1.004	7.601e+03	−1.006	1.007e+04
I_{39}	−1.010	7.398e+03	−1.008	8.888e+03
I_{40}	−1.015	5.069e+03	−1.013	6.302e+03

the nucleus, as opposed to being ionized elsewhere in the coma and then transported to *Rosetta* via another route.

Putting our results in the context of the spectra acquired by DFMS, we find that our results align with the DFMS observations. H_3O^+ and H_2O^+ were regularly detected during the entire mission period, with the largest counts observed near perihelion (Fuselier et al., 2015, 2016; Beth et al., 2016, 2020; Heritier et al., 2017a). DFMS scanned the range around 18 uq^{-1} three times more often as compared to the other mass ranges, though NH_4^+ was mostly detected during the higher outgassing period of the comet around perihelion (Beth et al., 2016, 2020). The ions $HCNH^+$, H_2COH^+ and $CH_3OH_2^+$ belonging to the HPA^+ ion group are also detected near perihelion in the DFMS high resolution (HR) spectra though the detection frequency is lower than that of NH_4^+ (Beth et al., 2020). This is to be expected, since NH_4^+ is the most abundant ion in the HPA^+ group, and 18 uq^{-1} is also scanned more often. Lewis et al. (2023) suggest that in addition to the protonation of NH_3, the dissociation of ammonium salts from cometary dust grains near DFMS may also be a source of NH_4^+. However, there is no evidence for the detection of H_3S^+, which is not understood. It may be related to the reduced energy acceptance of the instrument at higher uq^{-1} (Heritier et al., 2017a) or the suggested origin of H_2S from dust grains (Calmonte et al., 2016).

Beth et al. (2020) report on the detection of several of the ions belonging to the group PI_{other} for mass-per-charge ratio <40 uq^{-1}. We find CO^+ to be a primary contributor to PI_{other} in the time intervals of group 1, and it was detected in HR at $r_h > 2.2$ au pre-perihelion. CH_3OH^+ was detected in HR near perihelion, where we estimate it to have the most abundance, though there is no confirmed detection of O_2^+ at the same uq^{-1}. Beth et al. (2020) find peaks in low resolution (LR) at 27 uq^{-1} and 34 uq^{-1} near perihelion and post-perihelion at $r_h > 2.2$ au and these may be attributed to HCN^+ and H_2S^+ respectively, though they were not detected in HR. There is a weak signal corresponding to CH_4^+ in HR at $r_h > 2.2$ au post-perihelion. With regard to NH_3^+, Beth et al. (2020) clearly detect it near perihelion with higher counts than CH_3OH^+. Our models predict NH_3^+ to have a number density of a few cm^{-3} at the spacecraft location, and not as high as CH_3OH^+. We can explain this discrepancy in ion counts as follows. CH_3OH^+ has a mass-per-charge ratio of 32 uq^{-1} that is nearly double that of the mass-per-charge ratio of NH_3^+ (17 uq^{-1}). There is a reduction in the energy acceptance window of DFMS as the mass-per-charge ratio increases (Schläppi, 2011; Heritier et al., 2017a; Beth et al., 2020). Additionally, near perihelion, the ions are accelerated through a negative spacecraft potential, which further reduces the maximum energy that an ion can have in order to be detected by DFMS. We refer the reader to Heritier et al. (2017a) for a detailed analysis of the instrument sensitivity towards the detectable range of energies.

6. Conclusions

We have modeled the cometary ionosphere for 36 of the time intervals defined by Läuter et al. (2020), by using their neutral outgassing rates as inputs in our gas phase coma model. For most of the intervals, we find that our model-derived total ion densities can match the plasma densities measured by LAP/MIP within factors of 1–3 for group 1, 1–4 for group 2 (when UV extinction is included), and 2–3 for group 3. We further obtain the cometocentric distance variation of the density of the ions H_2O^+ and H_3O^+ and the ion groups HPA^+ and PI_{other}. We find that H_3O^+ is the most dominant ion at the location of *Rosetta*. In the intervals near perihelion, the HPA^+ ion group is dominant at low cometocentric distances. The PI_{other} ion group dominates over H_2O^+ at low cometocentric distances post-perihelion due to the rapid decline in the water production rate.

The deviations in our modeled ion densities from the plasma density measured by LAP/MIP can result due to several reasons. The variation in the local plasma density measured by *Rosetta* arises due to a host of factors which include day-night asymmetry, latitudinal variability, spacecraft maneuvers, and pickup by solar wind. Since the production rate within a particular time interval is fixed, the only variation that our model is able to capture is due to changes in the cometocentric distance location of the spacecraft. The production rates rely on the DFMS data for which Rubin et al. (2019) estimate a 30% uncertainty that may arise due to detector gain, sensitivity calibration, and fitting errors. Uncertainties in the production rates also arise due to the limited surface coverage which results in unknown emissions from not-seen surface elements. The photoemission current is seen to reduce near perihelion and this is attributed to the EUV extinction due to scattering by cometary nanograins (Johansson et al., 2017). Finally, the sublimation of volatiles from dust grains may also be an ion source in the coma, an effect which is not included in our model (Calmonte et al., 2016; Lewis et al., 2023).

CRediT authorship contribution statement

Sana Ahmed: Writing – review & editing, Writing – original draft, Methodology, Investigation, Formal analysis, Conceptualization. **Vikas Soni:** Visualization, Formal analysis.

Declaration of competing interest

The authors declare that they have no known competing financial interests or personal relationships that could have appeared to influence the work reported in this paper.

Data availability

Data will be made available on request.

Acknowledgments

The computations were performed on the Param Vikram-1000 High Performance Computing Cluster of the Physical Research Laboratory (PRL), India. The work done at PRL is supported by the Department of Space, Government of India. The data on the solar spectral UV fluxes was accessed via the LASP Interactive Solar Irradiance Datacenter (https://lasp.colorado.edu/lisird/). The photo-absorption cross sections are available at the PHIDRATES database (https://phidrates.space.swri.edu/). The time series data on the global volatile production rates was accessed via https://arxiv.org/abs/2006.01750. We express our gratitude to the ROSINA and RPC team, PI-ROSINA K. Altwegg (University of Bern, Switzerland), PI-LAP A. Eriksson (Swedish Institute of Space Physics, Uppsala, Sweden), and PI-MIP P. Henri (LPC2E/CNRS, Orléans, France). We thank R. Gill, E. P. G. Johansson, and F. L. Johansson for the Rosetta RPC-LAP archive of derived plasma parameters. We are grateful to Kinsuk Acharyya and Shashikiran Ganesh of PRL for useful insights and discussions. We thank the anonymous reviewers for their comments which strengthened this manuscript.

References

Ahmed, S., Acharyya, K., 2021. Gas-phase modeling of the cometary coma of interstellar comet 2I/Borisov. Astrophys. J. 923, 91. http://dx.doi.org/10.3847/1538-4357/ac2a42.

Balsiger, H., Altwegg, K., Bochsler, P., Eberhardt, P., Fischer, J., Graf, S., Jäckel, A., Kopp, E., Langer, U., Mildner, M., Müller, J., Riesen, T., Rubin, M., Scherer, S., Wurz, P., Wüthrich, S., Arijs, E., Delanoye, S., de Keyser, J., Neefs, E., Nevejans, D., Rème, H., Aoustin, C., Mazelle, C., Médale, J.L., Sauvaud, J.A., Berthelier, J.J., Bertaux, J.L., Duvet, L., Illiano, J.M., Fuselier, S.A., Ghielmetti, A.G., Magoncelli, T., Shelley, E.G., Korth, A., Heerlein, K., Lauche, H., Livi, S., Loose, A., Mall, U., Wilken, B., Gliem, F., Fiethe, B., Gombosi, T.I., Block, B., Carignan, G.R., Fisk, L.A., Waite, J.H., Young, D.T., Wollnik, H., 2007. Rosina Rosetta orbiter spectrometer for ion and neutral analysis. Space Sci. Rev. 128, 745–801. http://dx.doi.org/10.1007/s11214-006-8335-3.

Behar, E., Nilsson, H., Wieser, G.S., Nemeth, Z., Broiles, T.W., Richter, I., 2016. Mass loading at 67P/Churyumov-Gerasimenko: A case study. Geophys. Res. Lett. 43, 1411–1418. http://dx.doi.org/10.1002/2015GL067436, arXiv:1805.05587.

Berčič, L., Behar, E., Nilsson, H., Nicolaou, G., Stenberg Wieser, G., Wieser, M., Goetz, C., 2018. Cometary ion dynamics observed in the close vicinity of comet 67P/Churyumov-Gerasimenko during the intermediate activity period. Astron. Astrophys. 613, A57. http://dx.doi.org/10.1051/0004-6361/201732082.

Besse, S., Vallat, C., Barthelemy, M., Coia, D., Costa, M., De Marchi, G., Fraga, D., Grotheer, E., Heather, D., Lim, T., Martinez, S., Arviset, C., Barbarisi, I., Docasal, R., Macfarlane, A., Rios, C., Saiz, J., Vallejo, F., 2018. ESA's Planetary Science Archive: Preserve and present reliable scientific data sets. Planet. Space Sci. 150, 131–140. http://dx.doi.org/10.1016/j.pss.2017.07.013.

Beth, A., Altwegg, K., Balsiger, H., Berthelier, J.J., Calmonte, U., Combi, M.R., De Keyser, J., Dhooghe, F., Fiethe, B., Fuselier, S.A., Galand, M., Gasc, S., Gombosi, T.I., Hansen, K.C., Hässig, M., Héritier, K.L., Kopp, E., Le Roy, L., Mandt, K.E., Peroy, S., Rubin, M., Sémon, T., Tzou, C.Y., Vigren, E., 2016. First in-situ detection of the cometary ammonium ion NH_4^+ (protonated ammonia NH_3) in the coma of 67P/C-G near perihelion. Mon. Not. R. Astron. Soc. 462, S562–S572. http://dx.doi.org/10.1093/mnras/stw3370.

Beth, A., Altwegg, K., Balsiger, H., Berthelier, J.J., Combi, M.R., De Keyser, J., Fiethe, B., Fuselier, S.A., Galand, M., Gombosi, T.I., Rubin, M., Sémon, T., 2020. ROSINA ion zoo at Comet 67P. Astron. Astrophys. 642, A27. http://dx.doi.org/10.1051/0004-6361/201936775, arXiv:2008.08430.

Biver, N., Bockelée-Morvan, D., Hofstadter, M., Lellouch, E., Choukroun, M., Gulkis, S., Crovisier, J., Schloerb, F.P., Rezac, L., von Allmen, P., Lee, S., Leyrat, C., Ip, W.H., Hartogh, P., Encrenaz, P., Beaudin, G., MIRO Team, 2019. Long-term monitoring of the outgassing and composition of comet 67P/Churyumov-Gerasimenko with the Rosetta/MIRO instrument. Astron. Astrophys. 630, A19. http://dx.doi.org/10.1051/0004-6361/201834960.

Burch, J.L., Goldstein, R., Cravens, T.E., Gibson, W.C., Lundin, R.N., Pollock, C.J., Winningham, J.D., Young, D.T., 2007. RPC-IES: The ion and electron sensor of the Rosetta plasma consortium. Space Sci. Rev. 128, 697–712. http://dx.doi.org/10.1007/s11214-006-9002-4.

Calmonte, U., Altwegg, K., Balsiger, H., Berthelier, J.J., Bieler, A., Cessateur, G., Dhooghe, F., van Dishoeck, E.F., Fiethe, B., Fuselier, S.A., Gasc, S., Gombosi, T.I., Hässig, M., Le Roy, L., Rubin, M., Sémon, T., Tzou, C.Y., Wampfler, S.F., 2016. Sulphur-bearing species in the coma of comet 67P/Churyumov-Gerasimenko. Mon. Not. R. Astron. Soc. 462, S253–S273. http://dx.doi.org/10.1093/mnras/stw2601.

Carr, C., Cupido, E., Lee, C.G.Y., Balogh, A., Beek, T., Burch, J.L., Dunford, C.N., Eriksson, A.I., Gill, R., Glassmeier, K.H., Goldstein, R., Lagoutte, D., Lundin, R., Lundin, K., Lybekk, B., Michau, J.L., Musmann, G., Nilsson, H., Pollock, C., Richter, I., Trotignon, J.G., 2007. RPC: The Rosetta plasma consortium. Space Sci. Rev. 128, 629–647. http://dx.doi.org/10.1007/s11214-006-9136-4.

Chamberlin, P.C., Eparvier, F.G., Knoer, V., Leise, H., Pankratz, A., Snow, M., Templeman, B., Thiemann, E.M.B., Woodraska, D.L., Woods, T.N., 2020. The flare irradiance spectral model-version 2 (FISM2). Space Weather 18, e02588. http://dx.doi.org/10.1029/2020SW002588.

Combi, M., Shou, Y., Fougere, N., Tenishev, V., Altwegg, K., Rubin, M., Bockelée-Morvan, D., Capaccioni, F., Cheng, Y.C., Fink, U., Gombosi, T., Hansen, K.C., Huang, Z., Marshall, D., Toth, G., 2020. The surface distributions of the production of the major volatile species, H_2O, CO_2, CO and O_2, from the nucleus of comet 67P/Churyumov-Gerasimenko throughout the Rosetta Mission as measured by the ROSINA double focusing mass spectrometer. Icarus 335, 113421. http://dx.doi.org/10.1016/j.icarus.2019.113421, arXiv:1909.02082.

Cravens, T.E., Kozyra, J.U., Nagy, A.F., Gombosi, T.I., Kurtz, M., 1987. Electron impact ionization in the vicinity of comets. J. Geophys. Res. 92, 7341–7353. http://dx.doi.org/10.1029/JA092iA07p07341.

Edberg, N.J.T., Alho, M., André, M., Andrews, D.J., Behar, E., Burch, J.L., Carr, C.M., Cupido, E., Engelhardt, I.A.D., Eriksson, A.I., Glassmeier, K.H., Goetz, C., Goldstein, R., Henri, P., Johansson, F.L., Koenders, C., Mandt, K., Möstl, C., Nilsson, H., Odelstad, E., Richter, I., Simon Wedlund, C., Stenberg Wieser, G., Szego, K., Vigren, E., Volwerk, M., 2016a. CME impact on comet 67P/Churyumov-Gerasimenko. Mon. Not. R. Astron. Soc. 462, S45–S56. http://dx.doi.org/10.1093/mnras/stw2112, arXiv:1809.04981.

Edberg, N.J.T., Eriksson, A.I., Odelstad, E., Henri, P., Lebreton, J.P., Gasc, S., Rubin, M., André, M., Gill, R., Johansson, E.P.G., Johansson, F., Vigren, E., Wahlund, J.E., Carr, C.M., Cupido, E., Glassmeier, K.H., Goldstein, R., Koenders, C., Mandt, K., Nemeth, Z., Nilsson, H., Richter, I., Wieser, G.S., Szego, K., Volwerk, M., 2015. Spatial distribution of low-energy plasma around comet 67P/CG from Rosetta measurements. Geophys. Res. Lett. 42, 4263–4269. http://dx.doi.org/10.1002/2015GL064233, arXiv:1608.06745.

Edberg, N.J.T., Eriksson, A.I., Odelstad, E., Vigren, E., Andrews, D.J., Johansson, F., Burch, J.L., Carr, C.M., Cupido, E., Glassmeier, K.H., Goldstein, R., Halekas, J.S., Henri, P., Koenders, C., Mandt, K., Mokashi, P., Nemeth, Z., Nilsson, H., Ramstad, R., Richter, I., Wieser, G.S., 2016b. Solar wind interaction with comet 67P: Impacts of corotating interaction regions. J. Geophys. Res. (Space Phys.) 121, 949–965. http://dx.doi.org/10.1002/2015JA022147, arXiv:1809.05278.

Edberg, N.J.T., Eriksson, A.I., Vigren, E., Johansson, F.L., Goetz, C., Nilsson, H., Gilet, N., Henri, P., 2019. The convective electric field influence on the cold plasma and diamagnetic cavity of comet 67P. Astron. J. 158, 71. http://dx.doi.org/10.3847/1538-3881/ab2d28.

Eriksson, A.I., Boström, R., Gill, R., Åhlén, L., Jansson, S.E., Wahlund, J.E., André, M., Mälkki, A., Holtet, J.A., Lybekk, B., Pedersen, A., Blomberg, L.G., LAP Team, 2007. RPC-LAP: The Rosetta Langmuir probe instrument. Space Sci. Rev. 128, 729–744. http://dx.doi.org/10.1007/s11214-006-9003-3.

Eriksson, A.I., Engelhardt, I.A.D., André, M., Boström, R., Edberg, N.J.T., Johansson, F.L., Odelstad, E., Vigren, E., Wahlund, J.E., Henri, P., Lebreton, J.P., Miloch, W.J., Paulsson, J.J.P., Simon Wedlund, C., Yang, L., Karlsson, T., Jarvinen, R., Broiles, T., Mandt, K., Carr, C.M., Galand, M., Nilsson, H., Norberg, C., 2017. Cold and warm electrons at comet 67P/Churyumov-Gerasimenko. Astron. Astrophys. 605, A15. http://dx.doi.org/10.1051/0004-6361/201630159.

Fougere, N., Altwegg, K., Berthelier, J.J., Bieler, A., Bockelée-Morvan, D., Calmonte, U., Capaccioni, F., Combi, M.R., De Keyser, J., Debout, V., Erard, S., Fiethe, B., Filacchione, G., Fink, U., Fuselier, S.A., Gombosi, T.I., Hansen, K.C., Hässig, M., Huang, Z., Le Roy, L., Leyrat, C., Migliorini, A., Piccioni, G., Rinaldi, G., Rubin, M., Shou, Y., Tenishev, V., Toth, G., Tzou, C.Y., 2016. Direct Simulation Monte Carlo modelling of the major species in the coma of comet 67P/Churyumov-Gerasimenko. Mon. Not. R. Astron. Soc. 462, S156–S169. http://dx.doi.org/10.1093/mnras/stw2388.

Fuselier, S.A., Altwegg, K., Balsiger, H., Berthelier, J.J., Beth, A., Bieler, A., Briois, C., Broiles, T.W., Burch, J.L., Calmonte, U., Cessateur, G., Combi, M., De Keyser, J., Fiethe, B., Galand, M., Gasc, S., Gombosi, T.I., Gunell, H., Hansen, K.C., Hässig, M., Heritier, K.L., Korth, A., Le Roy, L., Luspay-Kuti, A., Mall, U., Mandt, K.E., Petrinec, S.M., Rème, H., Rinaldi, M., Rubin, M., Sémon, T., Trattner, K.J., Tzou, C.Y., Vigren, E., Waite, J.H., Wurz, P., 2016. Ion chemistry in the coma of comet 67P near perihelion. Mon. Not. R. Astron. Soc. 462, S67–S77. http://dx.doi.org/10.1093/mnras/stw2149.

Fuselier, S.A., Altwegg, K., Balsiger, H., Berthelier, J.J., Bieler, A., Briois, C., Broiles, T.W., Burch, J.L., Calmonte, U., Cessateur, G., Combi, M., De Keyser, J., Fiethe, B., Galand, M., Gasc, S., Gombosi, T.I., Gunell, H., Hansen, K.C., Hässig, M., Jäckel, A., Korth, A., Le Roy, L., Mall, U., Mandt, K.E., Petrinec, S.M., Raghuram, S., Rème, H., Rinaldi, M., Rubin, M., Sémon, T., Trattner, K.J., Tzou, C.Y., Vigren, E., Waite, J.H., Wurz, P., 2015. ROSINA/DFMS and IES observations of 67P: Ion-neutral chemistry in the coma of a weakly outgassing comet. Astron. Astrophys. 583, A2. http://dx.doi.org/10.1051/0004-6361/201526210.

Galand, M., Héritier, K.L., Odelstad, E., Henri, P., Broiles, T.W., Allen, A.J., Altwegg, K., Beth, A., Burch, J.L., Carr, C.M., Cupido, E., Eriksson, A.I., Glassmeier, K.H., Johansson, F.L., Lebreton, J.P., Mandt, K.E., Nilsson, H., Richter, I., Rubin, M.,

Sagnières, L.B.M., Schwartz, S.J., Sémon, T., Tzou, C.Y., Vallières, X., Vigren, E., Wurz, P., 2016. Ionospheric plasma of comet 67P probed by Rosetta at 3 au from the Sun. Mon. Not. R. Astron. Soc. 462, S331–S351. http://dx.doi.org/10.1093/mnras/stw2891.

Gasc, S., Altwegg, K., Fiethe, B., Jäckel, A., Korth, A., Le Roy, L., Mall, U., Rème, H., Rubin, M., Hunter Waite, J., Wurz, P., 2017. Sensitivity and fragmentation calibration of the time-of-flight mass spectrometer RTOF on board ESA's Rosetta mission. Planet. Space Sci. 135, 64–73. http://dx.doi.org/10.1016/j.pss.2016.11.011.

Gilet, N., Henri, P., Wattieaux, G., Cilibrasi, M., Béghin, C., 2017. Electrostatic potential radiated by a pulsating charge in a two-electron temperature plasma. Radio Sci. 52, 1432–1448. http://dx.doi.org/10.1002/2017RS006294.

Glassmeier, K.H., Richter, I., Diedrich, A., Musmann, G., Auster, U., Motschmann, U., Balogh, A., Carr, C., Cupido, E., Coates, A., Rother, M., Schwingenschuh, K., Szegö, K., Tsurutani, B., 2007. RPC-MAG the fluxgate magnetometer in the ROSETTA plasma consortium. Space Sci. Rev. 128, 649–670. http://dx.doi.org/10.1007/s11214-006-9114-x.

Goetz, C., Behar, E., Beth, A., Bodewits, D., Bromley, S., Burch, J., Deca, J., Divin, A., Eriksson, A.I., Feldman, P.D., Galand, M., Gunell, H., Henri, P., Heritier, K., Jones, G.H., Mandt, K.E., Nilsson, H., Noonan, J.W., Odelstad, E., Parker, J.W., Rubin, M., Simon Wedlund, C., Stephenson, P., Taylor, M.G.G.T., Vigren, E., Vines, S.K., Volwerk, M., 2022. The plasma environment of comet 67P/Churyumov-Gerasimenko. Space Sci. Rev. 218, 65. http://dx.doi.org/10.1007/s11214-022-00931-1.

Goetz, C., Tsurutani, B.T., Henri, P., Volwerk, M., Behar, E., Edberg, N.J.T., Eriksson, A., Goldstein, R., Mokashi, P., Nilsson, H., Richter, I., Wellbrock, A., Glassmeier, K.H., 2019. Unusually high magnetic fields in the coma of 67P/Churyumov-Gerasimenko during its high-activity phase. Astron. Astrophys. 630, A38. http://dx.doi.org/10.1051/0004-6361/201833544.

Haider, S.A., Bhardwaj, A., 2005. Radial distribution of production rates, loss rates and densities corresponding to ion masses ⩽40 amu in the inner coma of Comet Halley: Composition and chemistry. Icarus 177, 196–216. http://dx.doi.org/10.1016/j.icarus.2005.02.019, arXiv:astro-ph/0504667.

Hajra, R., Henri, P., Vallières, X., Galand, M., Héritier, K., Eriksson, A.I., Odelstad, E., Edberg, N.J.T., Burch, J.L., Broiles, T., Goldstein, R., Glassmeier, K.H., Richter, I., Goetz, C., Tsurutani, B.T., Nilsson, H., Altwegg, K., Rubin, M., 2017. Impact of a cometary outburst on its ionosphere. Rosetta Plasma Consortium observations of the outburst exhibited by comet 67P/Churyumov-Gerasimenko on 19 February 2016. Astron. Astrophys. 607, A34. http://dx.doi.org/10.1051/0004-6361/201730591.

Hansen, K.C., Altwegg, K., Berthelier, J.J., Bieler, A., Biver, N., Bockelée-Morvan, D., Calmonte, U., Capaccioni, F., Combi, M.R., de Keyser, J., Fiethe, B., Fougere, N., Fuselier, S.A., Gasc, S., Gombosi, T.I., Huang, Z., Le Roy, L., Lee, S., Nilsson, H., Rubin, M., Shou, Y., Snodgrass, C., Tenishev, V., Toth, G., Tzou, C.Y., Simon Wedlund, C., Rosina Team, 2016. Evolution of water production of 67P/Churyumov-Gerasimenko: An empirical model and a multi-instrument study. Mon. Not. R. Astron. Soc. 462, S491–S506. http://dx.doi.org/10.1093/mnras/stw2413.

Harder, J., Lawrence, G., Fontenla, J., Rottman, G., Woods, T., 2005. The spectral irradiance monitor: Scientific requirements, instrument design, and operation modes. Sol. Phys. 230, 141–167. http://dx.doi.org/10.1007/s11207-005-5007-5.

Henri, P., Vallières, X., Hajra, R., Goetz, C., Richter, I., Glassmeier, K.H., Galand, M., Rubin, M., Eriksson, A.I., Nemeth, Z., Vigren, E., Beth, A., Burch, J.L., Carr, C., Nilsson, H., Tsurutani, B., Wattieaux, G., 2017. Diamagnetic region(s): structure of the unmagnetized plasma around Comet 67P/CG. Mon. Not. R. Astron. Soc. 469, S372–S379. http://dx.doi.org/10.1093/mnras/stx1540.

Heritier, K.L., Altwegg, K., Balsiger, H., Berthelier, J.J., Beth, A., Bieler, A., Biver, N., Calmonte, U., Combi, M.R., De Keyser, J., Eriksson, A.I., Fiethe, B., Fougere, N., Fuselier, S.A., Galand, M., Gasc, S., Gombosi, T.I., Hansen, K.C., Hassig, M., Kopp, E., Odelstad, E., Rubin, M., Tzou, C.Y., Vigren, E., Vuitton, V., 2017a. Ion composition at comet 67P near perihelion: Rosetta observations and model-based interpretation. Mon. Not. R. Astron. Soc. 469, S427–S442. http://dx.doi.org/10.1093/mnras/stx1912.

Heritier, K.L., Galand, M., Henri, P., Johansson, F.L., Beth, A., Eriksson, A.I., Vallières, X., Altwegg, K., Burch, J.L., Carr, C., Ducrot, E., Hajra, R., Rubin, M., 2018. Plasma source and loss at comet 67P during the Rosetta mission. Astron. Astrophys. 618, A77. http://dx.doi.org/10.1051/0004-6361/201832881.

Heritier, K.L., Henri, P., Vallières, X., Galand, M., Odelstad, E., Eriksson, A.I., Johansson, F.L., Altwegg, K., Behar, E., Beth, A., Broiles, T.W., Burch, J.L., Carr, C.M., Cupido, E., Nilsson, H., Rubin, M., Vigren, E., 2017b. Vertical structure of the near-surface expanding ionosphere of comet 67P probed by Rosetta. Mon. Not. R. Astron. Soc. 469, S118–S129. http://dx.doi.org/10.1093/mnras/stx1459.

Hölscher, A., 2015. Formation of C3 and C2 in Cometary Comae (Ph.D. thesis). TU Berlin, URL: https://elib.dlr.de/96357/.

Huebner, W.F., Carpenter, C.W., 1979. Solar Photo Rate Coefficients. LA-8085-MS Informal Report, Los Alamos National Laboratory, Los Alamos, NM.

Huebner, W.F., Keady, J.J., Lyon, S.P., 1992. Solar photo rates for planetary atmospheres and atmospheric pollutants. Astrophys. Space Sci. 195, 1–294. http://dx.doi.org/10.1007/BF00644558.

Huebner, W.F., Mukherjee, J., 2015. Photoionization and photodissociation rates in solar and blackbody radiation fields. Planet. Space Sci. 106, 11–45. http://dx.doi.org/10.1016/j.pss.2014.11.022.

Itikawa, Y., 2002. Cross sections for electron collisions with carbon dioxide. J. Phys. Chem. Ref. Data 31, 749–767. http://dx.doi.org/10.1063/1.1481879.

Itikawa, Y., 2006. Cross sections for electron collisions with nitrogen molecules. J. Phys. Chem. Ref. Data 35, 31–53. http://dx.doi.org/10.1063/1.1937426.

Itikawa, Y., 2009. Cross sections for electron collisions with oxygen molecules. J. Phys. Chem. Ref. Data 38, 1–20. http://dx.doi.org/10.1063/1.3025886.

Itikawa, Y., 2015. Cross sections for electron collisions with carbon monoxide. J. Phys. Chem. Ref. Data 44, 013105. http://dx.doi.org/10.1063/1.4913926.

Itikawa, Y., Mason, N., 2005. Cross sections for electron collisions with water molecules. J. Phys. Chem. Ref. Data 34, 1–22. http://dx.doi.org/10.1063/1.1799251.

Johansson, F.L., Eriksson, A.I., Vigren, E., Bucciantini, L., Henri, P., Nilsson, H., Bergman, S., Edberg, N.J.T., Stenberg Wieser, G., Odelstad, E., 2021. Plasma densities, flow, and solar EUV flux at comet 67P. A cross-calibration approach. Astron. Astrophys. 653, A128. http://dx.doi.org/10.1051/0004-6361/202039959, arXiv:2106.15491.

Johansson, F.L., Odelstad, E., Paulsson, J.J.P., Harang, S.S., Eriksson, A.I., Mannel, T., Vigren, E., Edberg, N.J.T., Miloch, W.J., Simon Wedlund, C., Thiemann, E., Eparvier, F., Andersson, L., 2017. Rosetta photoelectron emission and solar ultraviolet flux at comet 67P. Mon. Not. R. Astron. Soc. 469, S626–S635. http://dx.doi.org/10.1093/mnras/stx2369, arXiv:1709.03874.

Kopp, G., Lawrence, G., Rottman, G., 2005. The total irradiance monitor (TIM): Science results. Sol. Phys. 230, 129–139. http://dx.doi.org/10.1007/s11207-005-7433-9.

Kramer, T., Läuter, M., Rubin, M., Altwegg, K., 2017. Seasonal changes of the volatile density in the coma and on the surface of comet 67P/Churyumov-Gerasimenko. Mon. Not. R. Astron. Soc. 469, S20–S28. http://dx.doi.org/10.1093/mnras/stx866, arXiv:1704.03874.

Läuter, M., Kramer, T., Rubin, M., Altwegg, K., 2019. Surface localization of gas sources on comet 67P/Churyumov-Gerasimenko based on DFMS/COPS data. Mon. Not. R. Astron. Soc. 483, 852–861. http://dx.doi.org/10.1093/mnras/sty3103, arXiv:1804.06696.

Läuter, M., Kramer, T., Rubin, M., Altwegg, K., 2020. The gas production of 14 species from comet 67P/Churyumov-Gerasimenko based on DFMS/COPS data from 2014 to 2016. Mon. Not. R. Astron. Soc. 498, 3995–4004. http://dx.doi.org/10.1093/mnras/staa2643, arXiv:2006.01750.

Lewis, Z.M., Beth, A., Altwegg, K., Galand, M., Goetz, C., Heritier, K., O'Rourke, L., Rubin, M., Stephenson, P., 2023. Origin and trends in NH_4^+ observed in the coma of 67P. Mon. Not. R. Astron. Soc. 523, 6208–6219. http://dx.doi.org/10.1093/mnras/stad1787.

Marshall, D.W., Hartogh, P., Rezac, L., von Allmen, P., Biver, N., Bockelée-Morvan, D., Crovisier, J., Encrenaz, P., Gulkis, S., Hofstadter, M., Ip, W.H., Jarchow, C., Lee, S., Lellouch, E., 2017. Spatially resolved evolution of the local H_2O production rates of comet 67P/Churyumov-Gerasimenko from the MIRO instrument on Rosetta. Astron. Astrophys. 603, A87. http://dx.doi.org/10.1051/0004-6361/201730502.

Nemeth, Z., 2020. The dynamics of the magnetic-field-free cavity around comets. Astrophys. J. 891, 112. http://dx.doi.org/10.3847/1538-4357/ab6e69.

Nemeth, Z., Timar, A., Szego, K., Henri, P., Hajra, R., Wattieaux, G., 2020. Plasma distribution around Comet 67P in the last month of the Rosetta mission. Icarus 350, 113924. http://dx.doi.org/10.1016/j.icarus.2020.113924.

Nilsson, H., Gunell, H., Karlsson, T., Brenning, N., Henri, P., Goetz, C., Eriksson, A.I., Behar, E., Stenberg Wieser, G., Vallières, X., 2018. Size of a plasma cloud matters. The polarisation electric field of a small-scale comet ionosphere. Astron. Astrophys. 616, A50. http://dx.doi.org/10.1051/0004-6361/201833199.

Nilsson, H., Lundin, R., Lundin, K., Barabash, S., Borg, H., Norberg, O., Fedorov, A., Sauvaud, J.A., Koskinen, H., Kallio, E., Riihelä, P., Burch, J.L., 2007. RPC-ICA: The ion composition analyzer of the Rosetta plasma consortium. Space Sci. Rev. 128, 671–695. http://dx.doi.org/10.1007/s11214-006-9031-z.

Nilsson, H., Stenberg Wieser, G., Behar, E., Simon Wedlund, C., Kallio, E., Gunell, H., Edberg, N.J.T., Eriksson, A.I., Yamauchi, M., Koenders, C., Wieser, M., Lundin, R., Barabash, S., Mandt, K., Burch, J.L., Goldstein, R., Mokashi, P., Carr, C., Cupido, E., Fox, P.T., Szego, K., Nemeth, Z., Fedorov, A., Sauvaud, J.A., Koskinen, H., Richter, I., Lebreton, J.P., Henri, P., Volwerk, M., Vallat, C., Geiger, B., 2015. Evolution of the ion environment of comet 67P/Churyumov-Gerasimenko. Observations between 3.6 and 2.0 AU. Astron. Astrophys. 583, A20. http://dx.doi.org/10.1051/0004-6361/201526142.

Nilsson, H., Wieser, G.S., Behar, E., Gunell, H., Wieser, M., Galand, M., Simon Wedlund, C., Alho, M., Goetz, C., Yamauchi, M., Henri, P., Odelstad, E., Vigren, E., 2017. Evolution of the ion environment of comet 67P during the Rosetta mission as seen by RPC-ICA. Mon. Not. R. Astron. Soc. 469, S252–S261. http://dx.doi.org/10.1093/mnras/stx1491.

Nilsson, H., Williamson, H., Bergman, S., Stenberg Wieser, G., Wieser, M., Behar, E., Eriksson, A.I., Johansson, F.L., Richter, I., Goetz, C., 2020. Average cometary ion flow pattern in the vicinity of comet 67P from moment data. Mon. Not. R. Astron. Soc. 498, 5263–5272. http://dx.doi.org/10.1093/mnras/staa2613.

Odelstad, E., Eriksson, A.I., Johansson, F.L., Vigren, E., Henri, P., Gilet, N., Heritier, K.L., Vallières, X., Rubin, M., André, M., 2018. Ion velocity and electron temperature inside and around the diamagnetic cavity of comet 67P. J. Geophys. Res. (Space Phys.) 123, 5870–5893. http://dx.doi.org/10.1029/2018JA025542, arXiv:1808.03581.

Preusker, F., Scholten, F., Matz, K.D., Roatsch, T., Hviid, S.F., Mottola, S., Knollenberg, J., Kührt, E., Pajola, M., Oklay, N., Vincent, J.B., Davidsson, B., A'Hearn, M.F., Agarwal, J., Barbieri, C., Barucci, M.A., Bertaux, J.L., Bertini, I., Cremonese, G., Da Deppo, V., Debei, S., De Cecco, M., Fornasier, S., Fulle, M., Groussin, O., Gutiérrez, P.J., Güttler, C., Ip, W.H., Jorda, L., Keller, H.U., Koschny, D., Kramm, J.R., Küppers, M., Lamy, P., Lara, L.M., Lazzarin, M., Lopez Moreno, J.J., Marzari, F., Massironi, M., Naletto, G., Rickman, H., Rodrigo, R., Sierks, H., Thomas, N., Tubiana, C., 2017. The global meter-level shape model of comet 67P/Churyumov-Gerasimenko. Astron. Astrophys. 607, L1. http://dx.doi.org/10.1051/0004-6361/201731798.

Rodgers, S.D., Charnley, S.B., 2002. A model of the chemistry in cometary comae: deuterated molecules. Mon. Not. R. Astron. Soc. 330, 660–674. http://dx.doi.org/10.1046/j.1365-8711.2002.05165.x.

Rottman, G., 2005. The SORCE mission. Sol. Phys. 230, 7–25. http://dx.doi.org/10.1007/s11207-005-8112-6.

Rubin, M., Altwegg, K., Balsiger, H., Berthelier, J.J., Combi, M.R., De Keyser, J., Drozdovskaya, M., Fiethe, B., Fuselier, S.A., Gasc, S., Gombosi, T.I., Hänni, N., Hansen, K.C., Mall, U., Rème, H., Schroeder, I.R.H.G., Schuhmann, M., Sémon, T., Waite, J.H., Wampfler, S.F., Wurz, P., 2019. Elemental and molecular abundances in comet 67P/Churyumov-Gerasimenko. Mon. Not. R. Astron. Soc. 489, 594–607. http://dx.doi.org/10.1093/mnras/stz2086, arXiv:1907.11044.

Schläppi, B., 2011. Ph.D. thesis. Universität Bern. Bern, Switzerland.

Schulz, R., 2009. Rosetta—one comet rendezvous and two asteroid fly-bys. Sol. Syst. Res. 43, 343–352. http://dx.doi.org/10.1134/S0038094609040091.

Simon Wedlund, C., Behar, E., Nilsson, H., Alho, M., Kallio, E., Gunell, H., Bodewits, D., Heritier, K., Galand, M., Beth, A., Rubin, M., Altwegg, K., Volwerk, M., Gronoff, G., Hoekstra, R., 2019. Solar wind charge exchange in cometary atmospheres. III. Results from the Rosetta mission to comet 67P/Churyumov-Gerasimenko. Astron. Astrophys. 630, A37. http://dx.doi.org/10.1051/0004-6361/201834881, arXiv:1902.04417.

Song, M.Y., Yoon, J.S., Cho, H., Itikawa, Y., Karwasz, G.P., Kokoouline, V., Nakamura, Y., Tennyson, J., 2015. Cross sections for electron collisions with methane. J. Phys. Chem. Ref. Data 44, 023101. http://dx.doi.org/10.1063/1.4918630.

Trotignon, J.G., Michau, J.L., Lagoutte, D., Chabassière, M., Chalumeau, G., Colin, F., Décréau, P.M.E., Geiswiller, J., Gille, P., Grard, R., Hachemi, T., Hamelin, M., Eriksson, A., Laakso, H., Lebreton, J.P., Mazelle, C., Randriamboarison, O., Schmidt, W., Smit, A., Telljohann, U., Zamora, P., 2007. RPC-MIP: the mutual impedance probe of the Rosetta plasma consortium. Space Sci. Rev. 128, 713–728. http://dx.doi.org/10.1007/s11214-006-9005-1.

Vigren, E., Altwegg, K., Edberg, N.J.T., Eriksson, A.I., Galand, M., Henri, P., Johansson, F., Odelstad, E., Tzou, C.Y., Vallières, X., 2016. Model-observation comparisons of electron number densities in the coma of 67P/Churyumov-Gerasimenko during january 2015. Astron. J. 152, 59. http://dx.doi.org/10.3847/0004-6256/152/3/59.

Vigren, E., André, M., Edberg, N.J.T., Engelhardt, I.A.D., Eriksson, A.I., Galand, M., Goetz, C., Henri, P., Heritier, K., Johansson, F.L., Nilsson, H., Odelstad, E., Rubin, M., Stenberg-Wieser, G., Tzou, C.Y., Vallières, X., 2017. Effective ion speeds at ∼200-250 km from comet 67P/Churyumov-Gerasimenko near perihelion. Mon. Not. R. Astron. Soc. 469, S142–S148. http://dx.doi.org/10.1093/mnras/stx1472.

Vigren, E., Edberg, N.J.T., Eriksson, A.I., Galand, M., Henri, P., Johansson, F.L., Odelstad, E., Rubin, M., Vallières, X., 2019. The evolution of the electron number density in the coma of Comet 67P at the location of Rosetta from 2015 November through 2016 March. Astrophys. J. 881, 6. http://dx.doi.org/10.3847/1538-4357/ab29f7, arXiv:1909.00639.

Vigren, E., Galand, M., 2013. Predictions of ion production rates and ion number densities within the diamagnetic cavity of comet 67P/Churyumov-Gerasimenko at perihelion. Astrophys. J. 772, 33. http://dx.doi.org/10.1088/0004-637X/772/1/33.

Wattieaux, G., Gilet, N., Henri, P., Vallières, X., Bucciantini, L., 2019. RPC-MIP observations at comet 67P/Churyumov-Gerasimenko explained by a model including a sheath and two populations of electrons. Astron. Astrophys. 630, A41. http://dx.doi.org/10.1051/0004-6361/201834872.

Weiler, M., 2007. Study of the Gas and Dust Activity of Recent Comets (Ph.D. thesis). Technischen Universität, Berlin, Germany.

Woods, T.N., Eparvier, F.G., Hock, R., Jones, A.R., Woodraska, D., Judge, D., Didkovsky, L., Lean, J., Mariska, J., Warren, H., McMullin, D., Chamberlin, P., Berthiaume, G., Bailey, S., Fuller-Rowell, T., Sojka, J., Tobiska, W.K., Viereck, R., 2012. Extreme ultraviolet variability experiment (EVE) on the solar dynamics observatory (SDO): Overview of science objectives, instrument design, data products, and model developments. Sol. Phys. 275, 115–143. http://dx.doi.org/10.1007/s11207-009-9487-6.

Woods, T.N., Rottman, G., Vest, R., 2005. XUV photometer system (XPS): Overview and calibrations. Sol. Phys. 230, 345–374. http://dx.doi.org/10.1007/s11207-005-4119-2.

Yoon, J.S., Song, M.Y., Han, J.M., Hwang, S.H., Chang, W.S., Lee, B., Itikawa, Y., 2008. Cross sections for electron collisions with hydrogen molecules. J. Phys. Chem. Ref. Data 37, 913–931. http://dx.doi.org/10.1063/1.2838023.